Quaternary Science Reviews 354 (2025) 109263

Contents lists available at ScienceDirect

Quaternary Science Reviews

journal homepage: www.elsevier.com/locate/quascirev

A high-resolution chronology for the archaeological deposits at Pinnacle Point 5–6, Western Cape Province, South Africa

Zenobia Jacobs [a,b,*], Panagiotis Karkanas [c], B. Patrick Fahey [d], Erich C. Fisher [e,f], Curtis W. Marean [d,f]

[a] School of Earth, Atmospheric and Life Sciences, University of Wollongong, Wollongong, Australia
[b] Australian Research Council Centre of Excellence for Australian Biodiversity and Heritage (CABAH), University of Wollongong, Wollongong, Australia
[c] M.H. Wiener Laboratory for Archaeological Science, American School of Classical Studies at Athens, Athens, Greece
[d] Institute of Human Origins, School of Human Evolution and Social Change, Arizona State University, PO Box 872402, Tempe, AZ, 85287-2402, USA
[e] Interdisciplinary Center for Archaeology and Human Behaviour, Universidade do Algarve, Faro, 8005-139, Portugal
[f] African Centre for Palaeoscience, Nelson Mandela University, Gqeberha, Eastern Cape, 6031, South Africa

ARTICLE INFO

Handling editor: Mira Matthews

Keywords:
Optically stimulated luminescence dating
Middle Stone Age
Human-environment interactions
Bayesian age modelling
Sea-level change
Palaeo-Agulhas Plain

ABSTRACT

Pinnacle Point Site 5–6 (PP5-6) is a key archaeological and paleoenvironmental site located on the edge of the Palaeo-Agulhas Plain along the southern Cape coast of South Africa. Construction of high-resolution chronologies for archaeological sites beyond the range of radiocarbon dating is challenging. Geochronological methods such as optical dating are hampered by the availability of applicable materials that are directly associated with the events of interest. Optical dating relies on assumptions made about time-dependent changes and is made up of a series of measurements each with its own random and systematic uncertainties that together make up the age estimates. In this study, we explicitly took on the challenge to systematically produce a high-resolution chronology for PP5-6 made up of 197 individual age estimates of which 169 were input into a Bayesian age model. PP5-6 is ideal because of its fine-scale stratigraphy and use of modern excavation techniques and detailed recording of stratigraphy and plotted finds. Excavations and dating took place concurrently over almost two decades to inform the dating strategy, contextualise sample choice and data analysis, and to bring the scales of analysis of different proxies closer together. Here we present the optical dating process, including sensitivity tests of our instruments, data analysis procedures and modelling approach. We then construct a final timeline for comparisons with other proxy data and interpretation of the sedimentary sequence and occupation of PP5-6 over an interval of ~60,000 years from ~110,000 to ~50,000 years ago. We show how closely linked sediment deposition is to changes in global climate and sea-level, identify a few Pleistocene and Holocene erosional events that modified the site post-depositionally and place a variety of interconnected causes and effects coincident with different types of occupation on this timeline. This approach opens up opportunities to reduce the resolution of chronologies closer to the human timescales required to improve our understanding of changes through time and to make more direct comparisons between other sites and proxies that contain similarly highly resolved archives of human occupation and change.

1. Introduction

The southern Cape coast of South Africa is florally diverse (Manning and Goldblatt, 2012; Allsopp et al., 2014; Cowling et al., 2015), sensitive to climatic and sea-level changes (Fisher et al., 2020; Marean et al., 2020; Göktürk et al., 2023), and rich in important archaeological and palaeontological finds (e.g., Henshilwood et al., 2002, 2014; Marean et al., 2007; Brown et al., 2012; Helm et al., 2020). It figures prominently in discussions about modern human origins (Marean, 2015; Wadley, 2015), making it a region of special interest to ecologists, Earth scientists, archaeologists and palaeoanthropologists alike.

Sedimentary and other deposits in open-air, cave/rockshelter and offshore settings along this coast preserve evidence of natural and anthropogenic processes of site formation, along with records of past environments ranging from Middle Pleistocene to Holocene in age (e.g., Bateman et al., 2004; Bar Matthews et al., 2010; Carr et al., 2010, 2016;

* Corresponding author. School of Earth, Atmospheric and Life Sciences, University of Wollongong, Wollongong, Australia.
E-mail address: zenobia@uow.edu.au (Z. Jacobs).

https://doi.org/10.1016/j.quascirev.2025.109263
Received 27 November 2024; Received in revised form 13 February 2025; Accepted 13 February 2025
Available online 20 February 2025

Roberts et al., 2012; Cawthra et al., 2018, 2020; Oestmo et al., 2014; Braun et al., 2020; Jacobs et al., 2020; Karkanas et al., 2020).

The broad brushstrokes of when certain events occurred have been reported for several sites, but not at the level of detail required to establish with precision the timing of sedimentation and human habitation at any particular site, the existence and duration of any temporal gaps in their sequences, or the correlation of site formation and occupation histories with environmental factors, including changes in sea level and climate. This is, in large part, due to the lack of precision of individual age estimates obtained by applicable geochronological methods, such as optical dating of sediment (e.g., Roberts et al., 2015; Murray et al., 2021).

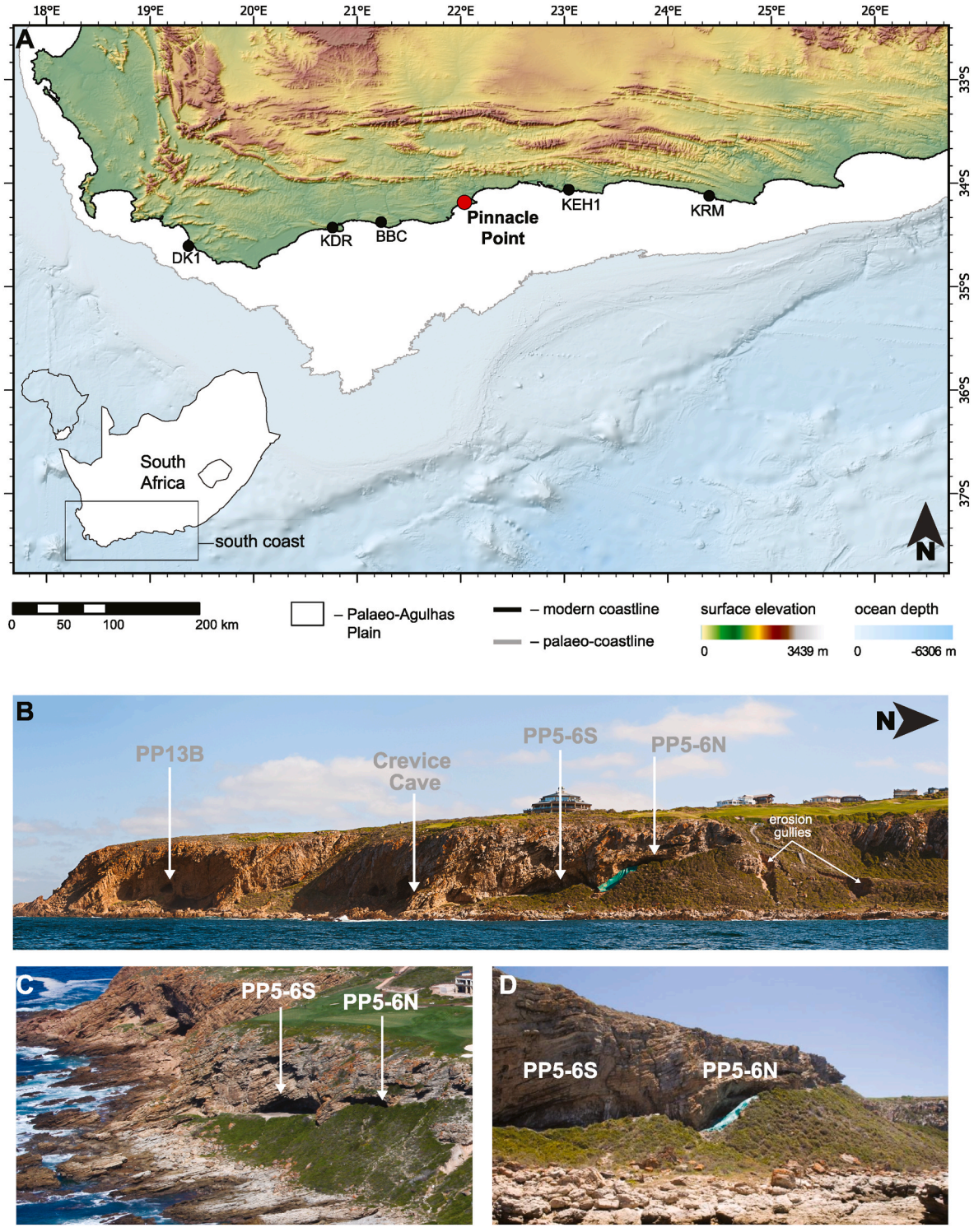

Fig. 1. **A,** Location of Pinnacle Point along the leading edge of one of a series of half-heart embayments along the southern Cape coast of South Africa. The maximum extent of the Palaeo-Agulhas Plain is shown in white using the −130 m isobath (Cawthra et al., 2020 and references therein). Surface and bathymetric data is from GEBCO Compilation Group (2023). Map datum: WGS84. **B,** Photograph showing the location of the Pinnacle Point site complex, including PP13B, Crevice Cave, PP5-6S, PP5-6N and two erosion gullies from which samples were collected in this study. **C,** and **D,** Photographs of PP5-6S and PP5-6N from two different angles and perspectives.

The use of modern and detailed excavation techniques, the recording of stratigraphy and plotted finds, and the preservation and exposure of fine-scale stratigraphy at the Pinnacle Point Site 5–6 (PP5-6) Site Complex afford a unique opportunity to test the capability of the optical dating technique to reconstruct, at high resolution, the chronology of this key Middle Stone Age (MSA) site. The discovery of glass shards associated with the Youngest Toba Tephra (YTT) in the sequence also provide independent age control and an accurate and precise isochron (Smith et al., 2018).

In this study, we expand on the previous chronological model developed for PP5-6N based on optically stimulated luminescence (OSL) dating of individual quartz grains from 90 samples (Smith et al., 2018). We add a further 79 samples collected from a series of vertical profiles that span the full extent of each large sedimentary unit (called stratigraphic aggregates) for optimal stratigraphic control and to fill in any gaps in our previous sampling. We also provide an initial sample set from the previously unreported cave of PP5-6S and report a series of age estimates for 28 sediment samples that provide insights into the history of deposition, erosion and re-deposition of sediments associated with debris flows, cut-and-fill sequences, and other geological features in and around PP5-6 (Karkanas et al., 2015).

The equivalent dose (D_e) values and environmental dose rates are estimated in a systematic way for all 197 samples to optimise consistency and to test the sensitivity of the D_e, dose rate and age estimates to different types of measurement and data-analysis procedures to identify any methodological problems. The final OSL ages for 169 samples, along with the astronomically calibrated $^{40}Ar/^{39}Ar$ age for the YTT (Storey et al., 2012), are then used to construct a Bayesian age model to constrain the timing and duration of anthropogenic- and geogenic-dominated phases of sediment deposition at the site. The resulting high-resolution chronology for the archaeological sequence shows that the deposits accumulated between approximately 110 and 50 thousand years ago (ka), spanning Marine Isotope Stage (MIS) 5 and MIS 4 and the start of MIS 3.

Our improved chronology for PP5-6N provides the basis for a detailed assessment of the archaeological record for a key period and region in which modern human technological innovations and symbolic behaviours flourished in a landscape undergoing major environmental changes (Marean et al., 2015; Marean et al., 2020). Furthermore, our chronology provides a template against which other archaeological, ecological, climatic, and geomorphological records for the southern Cape coast can be compared to elucidate the broader regional history of people, fauna, flora and landscapes during MIS 5, 4 and 3. This high-resolution chronology will form a robust timeline on which future publications of the PP5-6 behavioural, cultural, and environmental records will rest.

2. Site location and background

Pinnacle Point is a rocky headland where a series of caves, rockshelters and open-air localities are situated at the eastern edge of a half-heart embayment between the towns of Mossel Bay and Dana Bay on the southern Cape coast of South Africa (Fig. 1A). It is positioned on the northern edge of a broad and flat continental shelf (the Agulhas Bank). This bank would have been sub-aerially exposed to various extents during the Pleistocene as sea-levels fluctuated (e.g., Cawthra et al., 2020; Jacobs et al., 2020). During these times an extinct ecosystem was present known as the Palaeo-Agulhas Plain (Marean et al. 2014, 2020), and the Pinnacle Point sites, as well as others such as Die Kelders, Klipdrift, Blombos Cave, Knysna Eastern Heads 1 and Klasies River Mouth, would have looked out over this plain.

PP5-6 is part of the much larger Pinnacle Point Site Complex (Fig. 1b). PP5-6 is divided into two parts—PP5-6 North (PP5-6N) and PP5-6 South (PP5-6S) (Fig. 1B–D). PP5-6S is a cave with a boulder beach at its base at a height of ~+14 m asl, consistent with deposition during the sea-level highstand of MIS 11 (Roberts et al., 2012). MSA occupation overlies the boulder beach unconformably and is, in turn, overlain by a thick deposit of dune sand and lenses of clays and silts that choked the cave, sealing the archaeological remains until it was again re-opened during the Holocene.

PP5-6N is an east-facing rockshelter that is over 100 m long and was incised into the quartzitic Table Mountain Sandstone cliff face by multiple past high sea stands. The excavation has not reached bedrock, though auger testing revealed dune sand down to rock of unknown character. There is a significant accumulation of archaeological and geological sediments, ~30 m long and ~15 m high, revealed over the course of 12 years of archaeological excavation. These sediments are divided into 17 stratigraphic aggregates (Fig. 2) and 134 sub-aggregates (SubAggs). Each StratAgg is composed of multiple SubAggs, which are like 'layers' in most archaeological sites. A StratAgg is, therefore, essentially a packet of layers that represent deposits formed under similar processes or a set of depositional processes operating in a repetitive and consistent manner and that are constrained by major erosional unconformities or depositional discontinuities. The matrix of different StratAggs is dominated by aeolian, freefall roofspall/fault breccia and combustion features, resulting in a highly discernible stratigraphic succession. Table 2 in Karkanas et al. (2015) defines the different StratAggs and provides information about their approximate depths and main formation processes. A short description of each is provided in Supplementary Information, Section 3. There are, however, two important updates: (1) the erosional unconformity at the top of the LBSR and originally named Conrad Cobble and Sand (ALBS) is now its own StratAgg, called Cemented Rock and Sand (CRS), and (2) the 2016 and 2017 excavations at the northern end of the site revealed a much more laterally extensive and complex stratigraphy for the BAS (Black Ashy Sand) and BBCSR (Brown and Black Compact Sand and Roofspall), linking the previously isolated northwest remnant to the rest of the sequence. The latter two StratAggs were represented by a single StratAgg called BCSR in Karkanas et al. (2015). StratAggs and SubAggs are the two main units of analysis for the OSL dating study presented here.

Analyses of the archaeological finds at PP5-6 are ongoing, but they have so far revealed records of major changes in stone artefacts and raw material use that represent significant technological changes (Brown et al., 2009, 2012; Wilkins et al., 2017), variation in ochre procurement (McGrath et al., 2022), patterns in shellfish procurement that are closely linked to site-to-shore distances and types of coastal settings that match expected human behaviour (Cawthra et al., 2020), and palaeoenvironmental proxies (Esteban et al., 2020a, 2020b; Matthews et al., 2020).

3. Methods

Optically stimulated luminescence (OSL) dating was the main workhorse of this study. It was used to constrain the depositional ages of the geogenic and anthropogenic sediments (e.g., Huntley et al., 1985; Aitken, 1998; Jacobs and Roberts, 2007; Wintle, 2014; Roberts et al., 2015; Athanassas and Wagner, 2016; Murray et al., 2021). The method requires an estimate of the equivalent dose (D_e), determined from the OSL signal of quartz grains, and an estimate of the environmental dose rate, determined from the radioactivity of a sample and the material surrounding it to a distance of ~30 cm. The D_e divided by the environmental dose rate gives the burial time of the grains in calendar years ago. D_e values and environmental dose rates were estimated using the methods, equipment and procedures described and tested previously for samples from Pinnacle Point and elsewhere (e.g., Jacobs, 2010; Jacobs et al., 2019). Details are provided in Section 1 of Supplementary Information.

We collected 171 sediment samples from 17 StratAggs and 82 SubAggs at PP5-6N, and 5 samples from three StratAggs and five SubAggs in PP5-6S. We maximised the number of SubAggs from which a sample was collected to cover the maximum horizontal and vertical exposure of each StratAgg. The position of each sample along the north and east profiles

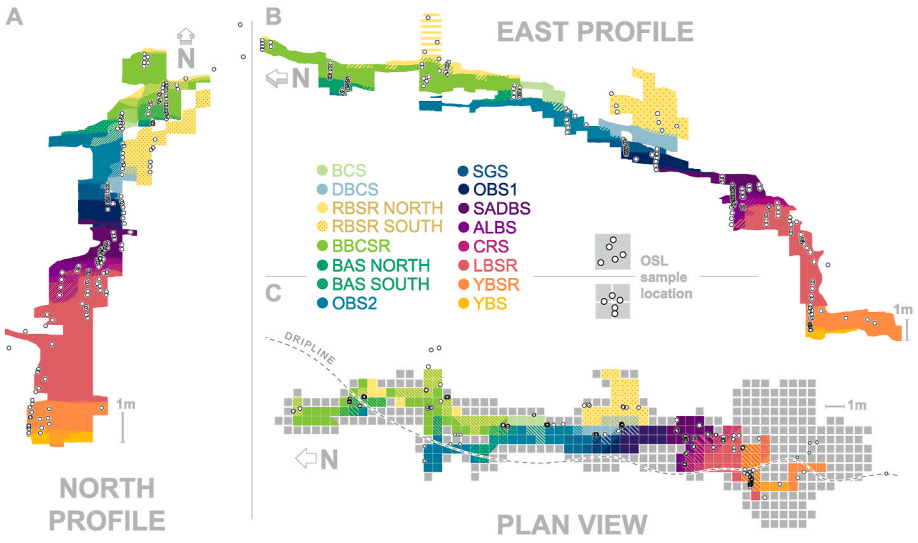

Fig. 2. Long Section stratigraphic silhouettes of the **A,** north and **B,** east profiles of PP5-6N showing the different StratAggs. Open circles indicate the location of each OSL sample. **C,** Plan view of PP5-6N showing the excavation grid, current dripline and StratAggs of the excavated squares and OSL sample locations.

of the site are shown in Fig. 2A and B and as plan view in Fig. 2C. An additional 21 samples were collected from three different types of deposits in and around the site: (1) cut-and-fill features (CAFF) in the upper and lower parts of PP5-6N, (2) dune sands from the erosion gullies to the north of PP5-6N (Fig. 1B) and a dune remnant cemented to the PP5-6N rockshelter wall, where a (3) remnant of cemented colluvium was also sampled (Fig. S14).

Sampling occurred during most field seasons between 2005 and 2017, which meant that any new SubAggs and StratAggs could be sampled as they were exposed, and that sampling was well-informed by the concurrent excavations and study of the sediments and site formation processes. Each sample was collected in consultation with the site director and geologist. This ensured that, at completion of excavations in 2017, a comprehensive set of samples had been collected with optimal stratigraphic control. A MAP (Mossel Bay Archaeological Project) sample number was assigned to each sample in the field. The position of each sample was recorded using Total Stations that provide millimetre accuracy for precise correlation to other finds and features. The location data were then integrated into an ArcGIS 10.x geodatabase that includes other data such as plotted finds, photography, and stratigraphic observations (Marean, 2010; Bernatchez and Marean, 2011; Fisher et al., 2015).

4. Results

The results of all samples are discussed together below to highlight average patterns and trends. Comparisons of results are often presented as Oldham plots (Oldham, 1962) using the natural logarithms of the D_e, dose rate and age estimates. An Oldham plot shows the difference between the log values of both pairs of data that are compared as a function of the mean log value of both pairs. We used the natural logarithms of the values for comparisons, following Galbraith and Roberts (2012), because the size of the standard errors increases in proportion to the D_e, dose rate and age by the same multiplicative factor. Variations can also be more easily interpreted on a log scale. Where the datasets are derived from different data, the 2σ errors are shown and include only the unshared components of error. Where comparisons are made on datasets that are derived from the same or some of the same data, no individual error bars are shown, because their estimation errors are correlated to an unknown degree. In such cases, the standard deviation of the differences gives an estimate of the individual standard error, assuming it is approximately the same for each data pair. This standard deviation is shown as a grey band in the plots calculated from the 97.5 percentage point of the t-distribution for the relevant number of degrees of freedom (equivalent to 1.96 for a normal distribution), so that any point within this band has a 95% confidence interval for the true difference that includes zero.

In all other graphs, the values are plotted as unlogged estimates and the errors are presented at 1σ and include all (shared and unshared) components.

Different colours are used to indicate samples from different StratAggs and these are applied to all figures. A colour legend is provided in Fig. 2.

4.1. Equivalent dose (D_e)

The final D_e values and their 1σ uncertainties for 169 samples from PP5-6N and PP5-6S are provided in Table S1 and for all 'other' contexts (including six samples from StratAggs BCS and DBCS) in Table S2, together with the overdispersion (OD) value and statistical model used to combine individual D_e values into a single D_e value for age determination. The error includes all known systematic and random errors. Below we present some key results that underpin these final D_e values and sensitivity tests that validate the results.

4.1.1. Between-instrument comparison

Five different luminescence readers (R2, R3, R4, R5 and R6) were used in the measurement of 220,800 individual grains from 196 samples; 5%, 39%, 24%, 7% and 25% of grains were measured on each of the different machines, respectively. It is important to ensure that there are no systematic differences between the different machines. We measured 8 samples, one each from 8 different StratAggs, on at least 3 of the machines; 1000 grains were measured on each machine for each sample and the measurement parameters were held constant across all machines. We used the statistical (homogeneity) test of Galbraith (2003) to determine if the independent D_e values obtained for each sample (Fig. 3) are self-consistent. The test assumes that the D_e values are independent observations sampled from a normal distribution, and the null hypothesis is that the D_e values are consistent with a common value. The calculated *P*-values indicate the probability that a random value from a chi-squared distribution with n-1 degrees of freedom is greater than the homogeneity statistic, *G*. The *P*-values are all >0.05, which supports the null hypothesis and suggest that the D_e values are self-consistent between instruments.

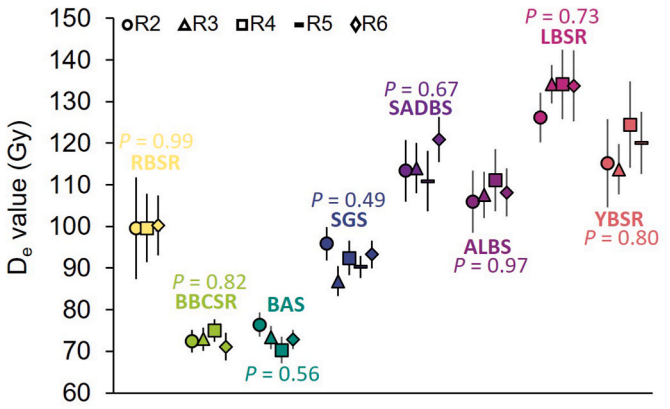

Fig. 3. Between-instrument reproducibility of D_e values for 8 samples from 8 different StratAggs.

4.1.2. Grain rejection

Of the 220,800 individual quartz grains measured, only 17,995 (8.2%) grains passed all rejection criteria for which reliable D_e values could be calculated. The numbers of grains measured and rejected are summarised in Table S3 and reasons for rejection are provided in Section 1.3 in Supplementary Information. Most grains in most samples (median = 78%) were rejected because grains emitted a negligible luminescence signal (criterion 1). The range of values (36–96%), however, varies significantly between samples, even within a StratAgg (Fig. 4A). There appears to be a correlation between samples collected from SubAggs with and without evidence of combustion features. The former return, on average, a higher number of grains with detectable OSL signals, likely due to thermal sensitization of the OSL signal (e.g., Chen et al., 2001; Jacobs et al., 2008b).

For grains that passed criteria 1–5 (Table S3), a relatively large proportion then failed because their L_n/T_n ratios (i.e., sensitivity-corrected luminescence signals; see Section 1.3 in Supplementary Information) lay at or above the asymptote (so-called dose saturation level) of the dose response curve, so a D_e value could not be obtained (criteria 6–7). The proportion of such grains ranges from 0% to 52% and is shown for each sample in each StratAgg in Fig. 4B. It is unknown whether these grains are derived from the *in situ* disintegration of the sandstone roofspall, or whether they represent grains with OSL signals that reach dose saturation much earlier than others with the same depositional and burial history (e.g., Li et al., 2020). It is well known that different quartz grains from the same sample exhibit a range of different dose response curve shapes and characteristic saturation dose (D_0) values (e.g., Roberts et al., 1999; Duller et al., 2000; Jacobs et al., 2006).

4.1.3. Single grain and multi-grain D_e comparisons

To test that single grain measurements and analytical processes, such as grain rejection, do not adversely impact the final D_e value, we measured 47 samples that display single component single-grain D_e distributions, using both single grains and multi-grain aliquots. These samples are from a range of different StratAggs, cover the full range of expected D_e values (~50–150 Gy) and proportion of 'saturated' grains (0–49%; Fig. 4B). All multi-grain aliquots were measured on the same machine (R2). The comparisons are presented in Fig. 5. On average there is no difference between the two data sets (mean difference = −0.004 ± 0.017). Six individual samples, however, have log D_e values that differ

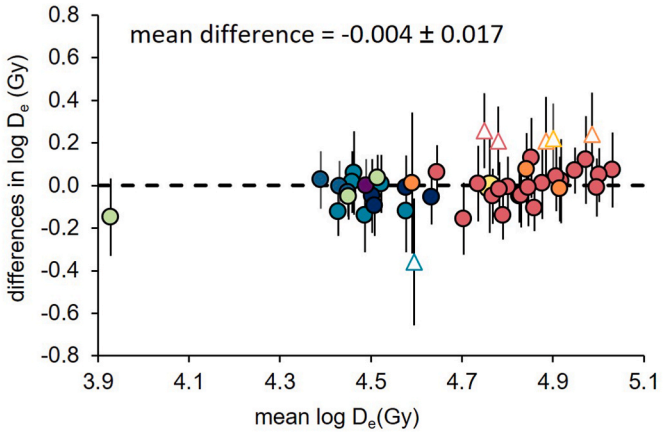

Fig. 5. Comparison of single grain and multi-grain aliquot D_e values calculated as the difference between each pair of log D_e values (single aliquot minus single grain; vertical axis) against the mean log D_e value of the pair (horizontal axis). Error bars are at 2σ calculated from the standard errors for each pair of observations. The open triangles represent samples with mean log D_e values that are >2σ different from zero.

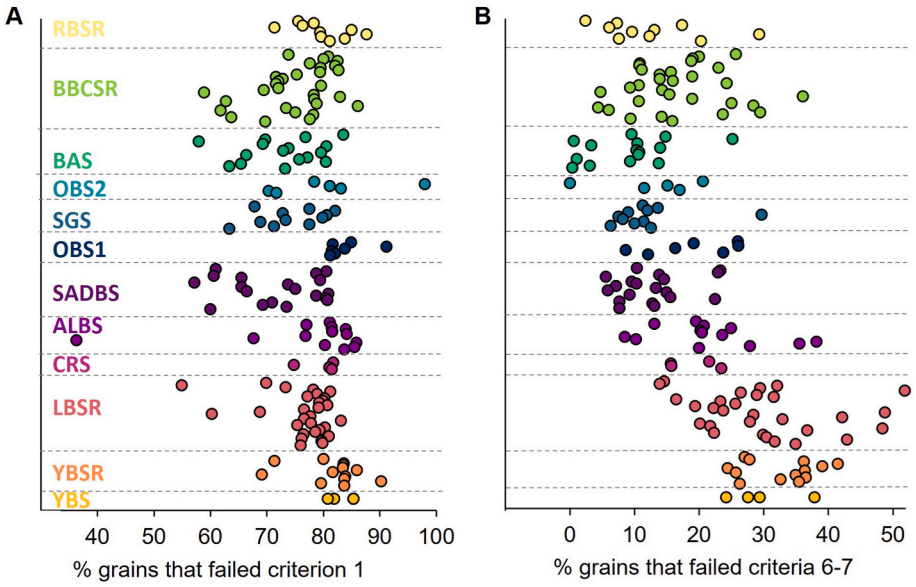

Fig. 4. Percentage of grains in each StratAgg in PP5-6N that failed **A,** criterion 1 (inherent OSL brightness) and **B,** criteria 6 and 7 (dose saturation).

by more than 2σ from a difference of 0 Gy (shown as open triangles); this includes a sample from OBS2 (162518), two samples each from LBSR (46794 and 46793) and YBSR (162756 and 162858), and one sample from YBS (162755). The single-grain data from the OBS2 sample is based on only nine imprecise D_e values and is considered unreliable. The difference between datasets for the other five samples suggests that the rejection of 'saturated' grains (Fig. 4B) may result in the truncation of the single-grain D_e distribution of some of the samples, which will lead to underestimation of the final D_e value.

4.1.4. *Calculation of D_e values using the L_nT_n method*

To further explore the possible effect that rejection of 'saturated' grains may have on the estimation of D_e, we systematically compared the single grain D_e values estimated using the conventional SAR approach (Section 1.3.1 in Supplementary Information) to those calculated from the same datasets using the L_nT_n method of Li et al. (2017, 2020; Section 1.3.2 in Supplementary Information). The latter method does not reject any 'saturated' grains, so a full and untruncated distribution of L_n/T_n ratios is included in the final D_e value (Li et al., 2020).

We first compared the multi-grain aliquot and L_nT_n-derived D_e values for the same samples focusing on the LBSR, YBSR and YBS StratAggs (Fig. 6A). Both datasets include all grains (including 'saturated' grains) so should give consistent results if all grains in the sample had the same burial history. The mean difference between the two pairs of D_e values for all samples (N = 27) is −0.090 ± 0.024 (standard deviation = 0.12). If the one clear outlier (162658) is excluded, then the mean difference is −0.071 ± 0.015, indicating that the L_nT_n method results in D_e values that are on average ~7% larger than those from the multi-grain aliquots. The five samples for which statistical differences are observed in Fig. 5 between the single grain and single aliquot D_e values are also shown here as open triangles; the single aliquot D_e values for these five samples are consistent with their respective single grain L_nT_n D_e values, which suggests that the corresponding conventional SAR single grain D_e values for these samples are underestimates of the sample D_e.

We next compared the single grain SAR and L_nT_n-derived D_e values for the same set of samples from LBSR, YBSR and YBS (Fig. 6B). As both datasets are using the same data, individual errors bars cannot be shown. Instead, the 95% confidence interval (shown as a grey bar) was calculated from the standard deviation of the differences (excluding sample 162658). Most D_e values (i.e., 20 of 27 samples) are consistent with there being no difference at 2σ, but five samples shown as open triangles have significantly different single grain SAR and L_nT_n D_e values. Because a statistically significant difference is obtained between the two single grain methods, but the multi-grain and L_nT_n D_e values are consistent, we infer that the conventional single grain SAR D_e distributions for these five samples are truncated and the final D_e values are, therefore, underestimated. For such samples, the multi-grain and L_nT_n D_e values would be more reliable. Where both estimates are available our preference is for the multi-grain D_e values as those are more precise and estimation of D_e more straightforward. To obtain more precise L_nT_n D_e values will require measurement of many more grains.

We also compared the single-grain SAR and L_nT_n D_e values for all samples for which both methods could be used (Fig. 6C; N = 171). Sixteen samples (10.5%) lie outside the grey band (Fig. 6C); these are

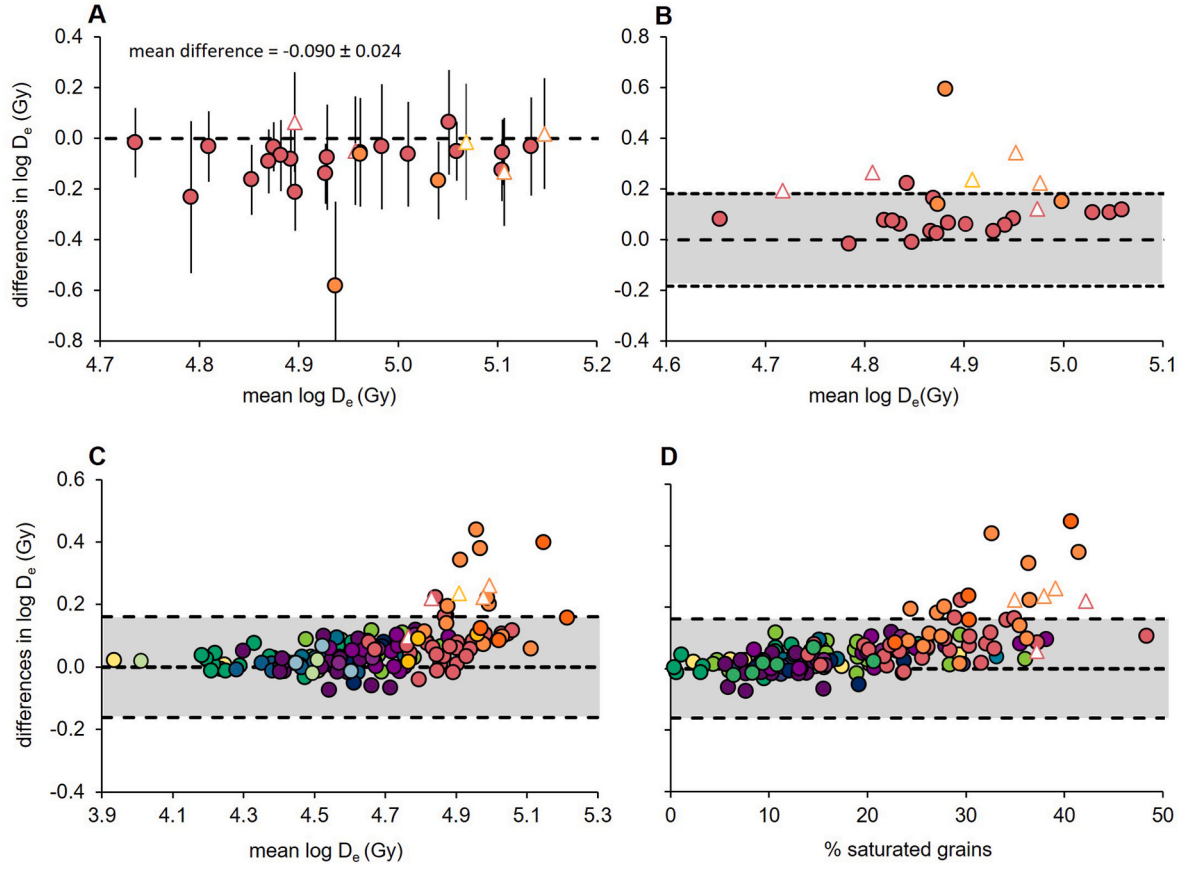

Fig. 6. **A,** Comparison of 27 multi-grain aliquot and single grain L_nT_n D_e estimates for the same samples as in Fig. 5 from LBSR, YBSR and YBS. Differences and errors calculated in the same way as in Fig. 5. **B,** Comparison of the same 27 samples as in **A**, but as the difference between L_nT_n minus conventional single grain SAR D_e values from the same dataset. The grey band denotes ±2.06 standard deviations about zero for individual differences (with 26 degrees of freedom). **C,** Same as **B**, but for 171 samples from 17 StratAggs in PP5-6N and four samples from PP5-6S. The grey band denotes ±1.97 standard deviations about zero for individual differences (with 170 degrees of freedom). **D,** Same data as in **C**, but shown as a function of the % saturated grains in a sample (see Fig. 4B). The open triangles in all plots are the same as in Fig. 5 (i.e., those that have conventional single grain SAR and multi-grain aliquot D_e values that are >2σ different).

from the oldest deposits in YBSR (N = 8), PP5-6S (N = 3), LBSR (N = 4) and YBS (N = 1) and include four of the five samples shown as triangles. There is also a strong correlation with the proportion of saturated grains. Fig. 6D shows the same data as Fig. 6C, but this time as a function of the proportion of 'saturated' grains (Fig. 4B). Samples with the largest proportion of 'saturated' grains also have the biggest differences in D_e. We infer from these data that the conventional SAR D_e distributions for those 16 samples are truncated and that their single grain D_e values are significantly underestimated. L_nT_n-derived D_e values should provide more accurate estimates of sample D_e and will be used for age determination for those samples that do not have multi-grain D_e values.

Conventional SAR D_e values are considered reliable for the remaining 155 samples and are used for final age determination. We remain cautious in our use of the L_nT_n method and multi-grain method as neither method can identify roofspall contamination.

4.1.5. *Single grain D_e distributions*

Three typical D_e distributions for samples in this study are displayed as radial plots in Fig. 7A–C. Most distributions suggest that the sediments were well-bleached prior to deposition and have remained undisturbed since burial. This is expected for a sequence with clear stratigraphy and no evidence of post-depositional disturbance at the sample locations. Three different statistical models were used to calculate a final D_e value. (1) The central age model (CAM) of Galbraith et al. (1999), which assumes a random distribution of D_e values around a central value (Fig. 7A) and that considers any overdispersion (OD) present (Tables S1 and S2). (2) The normalised median absolute deviation (nMAD) method (Powell et al., 2002; Rousseeuw et al., 2006) to identify outliers, using 1.4826 as the appropriate correction factor for a normal distribution. Log D_e values with nMADs >3 were rejected prior to application of the CAM (Fig. 7B); outliers are shown as open triangles. The OD values obtained for each sample, and the numbers of grains rejected after application of nMAD, are provided in brackets in Tables S1 and S2. The CAM and nMAD CAM were also used in the same way to calculate D_e values using the L_nT_n method. (3) The finite mixture model (FMM) of Roberts et al. (2000) was used for 13 samples that displayed two or more discrete D_e components (Fig. 7C). The optimal number of components and OD of the components were determined using the approach described in Galbraith and Roberts (2012). Eleven of these samples were from cut-and-fill features. The number of D_e components, OD values and proportion of grains represented by each component are listed in Table S2.

4.2. *Environmental dose rate*

The beta, gamma, cosmic and total environmental dose rates estimated for each sample are provided in Tables S1 and S2, together with the measured (prevailing) moisture contents and those used for final age determination.

4.2.1. *Beta dose rate*

Beta dose rates range from 0.32 ± 0.02 (571361, BAS) to 1.29 ± 0.04 (571383, BBCSR) Gy/ka, but range between 0.50 and 1.00 Gy/ka for the vast majority (95%) of samples. In general, higher values appear to be associated with roof spall-rich SubAggs (e.g., LBSR and YBSR) or the dark organic-rich layers found in BBCSR. The beta dose rates of most samples (N = 170) were calculated using two different methods—GM-25-5 beta counting and ICP-MS/OES. Comparisons of the results are displayed in Fig. 8A. Forty-two (25%) of the samples have beta dose rates that differ by more than 2σ from a difference of 0 Gy/ka, and the beta dose rates derived from ICP-MS/OES measurements are, on average, 1.5% lower compared to the GM-25-5 beta counting dose rates. We note that this is the opposite systematic trend to that observed for a similarly large dataset of samples from Denisova Cave in Siberia, which were measured using the same instruments and identical sample preparation procedures (Jacobs et al., 2019). The systematic difference observed here, therefore, is unlikely to be related to the instrumental set-up. A systematic effect was detected for a subset of the samples measured in 2007 and 2008, and these samples were re-measured in this study.

There is no *a priori* reason for the two measurement types to be identical. GM-25-5 beta counting detects all nuclear disintegrations that emit a beta particle from the U and Th decay chains (and from the decay of ^{40}K), whereas the dose rates obtained from the ICP-MS data are based on measurements of parental U and Th concentrations and assume secular equilibrium in the decay chains. Any disequilibrium, which is commonplace in the natural environment, will lead to differences in the dose rates obtained from these two methods. The difference observed here, therefore, is more likely to be related to differences in the geochemical properties of the sediment.

To explore this further, we calculated the beta dose rate for 37 samples derived from only U and Th using the elemental values obtained from ICP-MS and comparing those to the values obtained from thick-source alpha counting (TSAC) (Fig. 8B). The difference between the mean log beta dose rates so obtained is −0.20 ± 0.03. The ICP-MS dose rates are, therefore, smaller, on average, by ~20%, which supports the notion that some disequilibrium is present in the sediments. Using the ICP-MS elemental data for all samples, we calculate that, on average, 58 ± 0.4%, 20 ± 0.2% and 23 ± 0.3% of the beta dose rate derives from K, Th and U, respectively, so any disequilibrium in the uranium series will have a relatively small effect on the total beta dose rate.

We also tested the sensitivity of our age estimates to the use of beta dose rates derived in different ways (Fig. 8A). The external beta dose rate represents, on average, ~53% (±5% standard deviation) of the total environmental dose rate. If the beta dose rates are calculated using the ICP-MS/ICP-OES data, rather than the GM-25-5 beta counting data, then

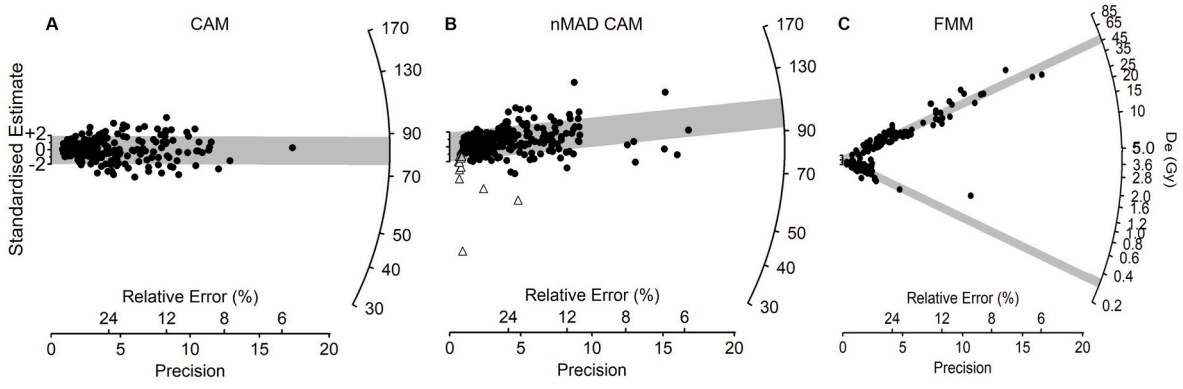

Fig. 7. Three types of representative single-grain D_e distributions observed for samples in this study for which the **A,** CAM (sample 46786, SADBS), **B,** nMAD CAM (sample 162508, SADBS) and **C,** FMM (sample 571367) were used to obtain the final weighted mean D_e value for age determination.

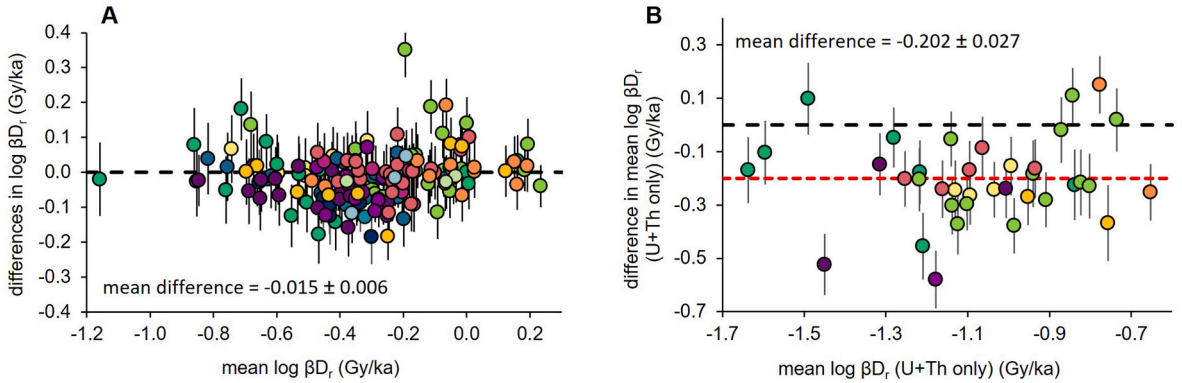

Fig. 8. A, Comparison of beta dose rates obtained from two different methods: GM-25-5 beta counting and ICP-MS/OES. The difference between each pair of log β_{Dr} values (vertical axis) is plotted as a function of the mean log β_{Dr} of the pair (horizontal axis). **B,** Comparison of the beta dose rates calculated from U and Th only using elemental values obtained from ICP-MS and TSAC. Error bars are at 2σ calculated from the theoretical standard errors for each pair of observations. The red stippled line shows the average mean difference for all samples. (For interpretation of the references to colour in this figure legend, the reader is referred to the Web version of this article.)

the ages will be, on average, ~1.2% (±4.4% standard deviation) older than those listed in Table S1. Such differences are well within the total uncertainties on the individual ages.

4.2.2. *Gamma dose rate*

Gamma dose rates range from 0.32 ± 0.01 (557334, OBS2) to 0.74 ± 0.03 (388702, BBCSR) Gy/ka. The gamma dose rates for 150 samples were measured directly using a field gamma spectrometer, which considers any dose rate inhomogeneity within a ~30 cm sphere around the sample. Field gamma spectrometry also has the advantage that it measures radionuclides lower down the uranium decay chain (from where most of the gamma radiation originates), so it is less susceptible to disequilibrium in the upper part of the chain. To demonstrate the importance of measuring the gamma dose rate directly, the gamma dose rate derived from ICP-MS/OES measurements of U, Th and K are compared with the directly measured gamma dose rates in Fig. 9A. As expected, there is a broad range of differences randomly distributed around a difference of 0 Gy/ka, but no systematic trend is evident. The average difference across all samples is 0.039 ± 0.018, so the field spectrometry values are, on average, 4 ± 2% larger than those derived from ICP-MS/OES.

The *in situ* gamma dose rates for a subset of samples (N = 37) were measured twice, in different years, as a test of reproducibility. The comparison is shown in Fig. 9B. There are five outliers (those outside the grey band): four of these samples were measured in 2010 (the only samples measured that year) and again in 2011. Inspection of the data shows severe contraction of the energy spectra, so the 2010 data are considered unreliable and have not been used for dose rate or age determination. The remaining measurement pairs are consistent with no significant difference (mean of 0.012 ± 0.010 after removing the five outliers), with any variations likely due to small differences in soil moisture content and/or use of different spectrometers.

4.3. *Individual age estimates*

Final ages for 169 samples from 15 of 17 StratAggs in PP5-6N and two StratAggs in PP5-6S are presented in Table S1. Uncertainties on the ages are given at 1σ (the standard error on the mean). Two estimates of uncertainty are shown in brackets after the ± symbol: the first (σ_1) is based on propagation of only the random (unshared) errors, while the second (σ_2) combines, in quadrature, both the unshared and systematic (shared) sources of error (see Section 4.4.3 for further discussion). The σ_1 errors (which range from 3.0% to 13.6% of the mean age; median = 5.3%) can be used for comparison with data generated within this study, whereas the σ_2 errors (which range from 3.9% to 13.9% of the mean age; median = 5.9%) should be used for comparisons with independent chronologies and with OSL ages obtained in other studies.

Age estimates range from 120 ± (16, 17) ka for the oldest sample in PP5-6S (571339) and 111 ± (8, 9) ka for the deepest sample in YBS in PP5-6N (571344) to 50 ± (2, 3) ka at the top of the sequence in the Geotrench in RBSR North (388692).

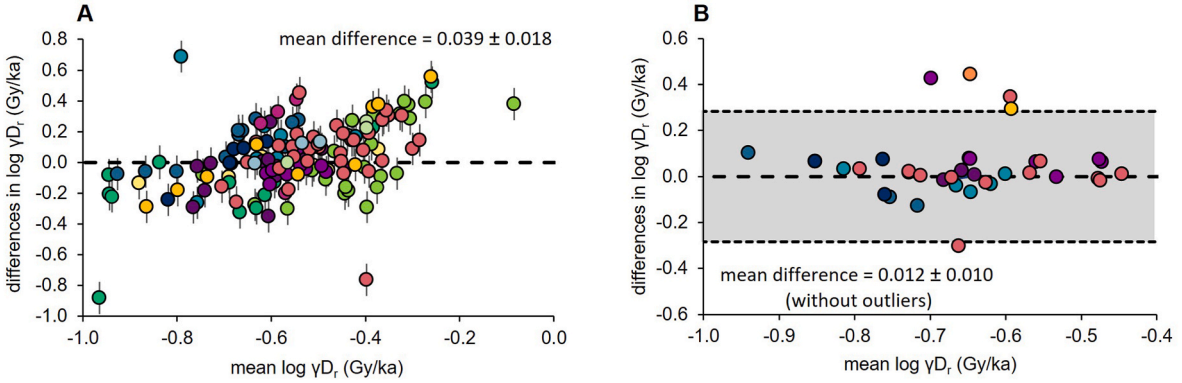

Fig. 9. A, Comparison of gamma dose rates obtained from two methods: field gamma spectrometry and ICP-MS/OES. Error bars are at 2σ calculated from the standard errors for each pair of observations. **B,** Comparison of the first and second field gamma spectrometry measurement of the gamma dose rate made at the same sample position but in different years. The grey band denotes ±2.03 standard deviations about zero for individual differences (with 36 degrees of freedom).

4.4. Bayesian age model and model tests

The 169 OSL ages in Table S1 were input into a Bayesian statistical age model using the OxCal platform (OxCal 4.4) (Bronk Ramsey, 2009a; Bronk Ramsey and Lee, 2013). Details about the model structure and parameters are provided in Section 2 in Supplementary Information together with the CQL code used to generate the model (Table S4). The full Bayesian modelled dataset is provided in Table S5, including age ranges at 68.2% and 95.4% prior (unmodelled) and posterior (modelled) probability.

The agreement indices of 226.4 (A_{model}) and 232.6 ($A_{overall}$) are much greater than the >60 acceptance threshold (Bronk Ramsey, 2009a) and indicate an excellent fit between the prior and posterior parts of the model. Fourteen samples had outlier probabilities of >5%. Six samples were assigned prior outlier probabilities of either 50% or 100% after their identification as significant outliers in an earlier iteration of the model. A further 8 samples returned posterior outlier probabilities of >5% (range 6–22%) in the final model; these samples were down-weighted accordingly in the final model. Prior and posterior outlier probabilities for all samples is listed in Table S5.

4.4.1. Boundary age estimates

A key outcome of the model is the estimation of posterior boundary age estimates for the start and end of each StratAgg in the sequence, represented by a probability distribution function. These estimates are highlighted in bold and italics in the grey rows in Table S5. Uncertainties associated with the *Transitional Boundaries* were calculated using the OxCal platform and are based on σ_1 (random) errors only. To incorporate the shared (systematic) errors in the estimates of total uncertainty, the mean posterior boundary ages at 95.4% probability are displayed in Fig. 10 with both σ_1 and σ_2 errors.

The entire sequence is constrained by an age of 109.0 ± (9.4, 9.8) ka for the *Start Boundary* at the base of the sequence in PP5-6S and an age of 51.6 ± (4.2, 5.0) ka for the *End Boundary* at the top of PP5-6N in RBSR North. These *Start* and *End Boundaries* are difficult to determine precisely, as they are only constrained on one side of the sequence.

Sedimentological observations suggest that sediment deposition in a geological sense in PP5-6N was probably continuous or nearly so. The only clear disconformities are at the lower contacts of BBCSR with underlying BAS, and the lower contacts of DBCS and BCS; the latter two StratAggs were not included in the model (see Section 2 in Supplementary Information). Contacts between adjoining StratAggs were, therefore, modelled as *Transitional Boundaries* where the end of one StratAgg is also the start of the next. The uncertainties on individual boundary age estimates range considerably through the sequence, with those in the middle of the sequence being much more precise (Fig. 10).

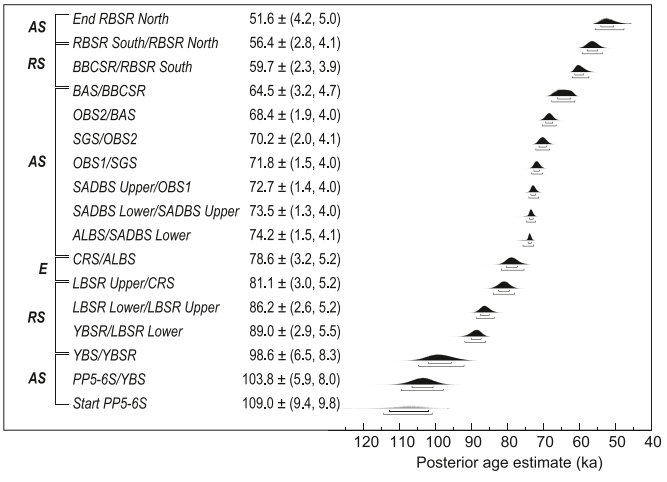

Fig. 10. Posterior boundary age estimates determined using a *Sequence* model in OxCal (see Section 2 in Supplementary Information). The brackets below the probability distributions of individual boundaries represent 68.2% and 95.4% confidence intervals. These were calculated in OxCal using the σ_1 errors on individual OSL age estimates. The mean ages of the 95.4% probability distributions are provided to the left together with two different total estimates of uncertainty, σ_1 and σ_2, in brackets. The deposits were divided into StratAggs that were either aeolian sand-dominated (AS), roofspall-dominated (RS) or representing an erosional unconformity (E).

4.4.2. Durations of stratigraphic aggregates

To quantify the possible duration of each StratAgg, we calculated their likely durations in calendar years using the *Interval* command in OxCal. This calculates the time difference between the modelled age estimates for the StratAgg *Boundaries* and assumes that the dated samples are drawn randomly from between them (i.e., distributed uniformly over its age range) (Bronk Ramsey et al., 2010). The durations so obtained for each StratAgg are listed in Table 1 at 68.2% and 95.4% probability. The 95.4% credible ranges for the durations are as short as 0–1640 years for SADBS Upper, and as long as 2400—15,950 years for YBSR. Only 6 of 16 StratAggs (YBSR, LBSR Upper, ALBS, BAS, BBCSR and RBSR South) each have durations that are >0 years at 95.4% probability (Table 1). This suggests that most of the StratAggs were potentially of relatively short duration.

4.5. Bayesian model sensitivity tests

We tested the sensitivity of our final age model (Model A) by running the same model two additional times, each with important differences: Model B does not include the high-precision $^{40}Ar/^{39}Ar$ age for the YTT, whereas Model C includes the YTT but the OSL ages are modelled with their full σ_2 errors.

4.5.1. Accuracy of OSL ages for Conrad Sand in ALBS

The YTT isochron is located within Conrad Sand in ALBS (Smith et al., 2018) and is precisely dated by $^{40}Ar/^{39}Ar$ dating to 73.88 ± 0.64 ka at 2σ (Storey et al., 2012). The difference between Models A and B can, therefore, test the accuracy of the prior and posterior ages for Conrad Sand in ALBS associated with the YTT. Fig. 11 shows a comparison of Model A and B results for Conrad Sand. Prior ages are shown as probability density functions in grey and the posterior estimates in purple; the YTT age is shown in red. Conrad Sand was modelled as a *Phase* within ALBS, so its *Start* and *End Boundary* posterior age estimates are shown in light purple, together with the *Transitional Boundary* estimate for ALBS/SADBS Lower in black.

Table 1
Bayesian modelled depositional durations for each StratAgg in years. Durations are shown for 68.2% and 95.4% probability calculated using the *Interval* command in OxCal.

StratAgg	Interval	
	68.2% probability	95.4% probability
RBSR North	1240—6280	0–8990
RBSR South	1920—5760	130–6980
BBCSR	1160—5950	50–8140
BAS	2060—6690	120–7620
OBS2	210–2620	0–3990
SGS	200–2230	0–3410
OBS1	0–1250	0–2300
SADBS Upper	0–830	0–1640
SADBS Lower	0–780	0–2270
ALBS	2950—6340	850–7470
CRS	0–3580	0–6430
LBSR Upper	2970—7020	940–8600
LBSR Lower	180–3640	0–6140
YBSR	6060—13,330	2400—15,950
YBS	0–6780	0–12,170
MBS and BYS	0–7380	0–15,030

Table 2
Comparison of modelled boundary ages from three different models. The relative errors for Models A and B were calculated from the unshared-only (modelled; σ_1) and full (unshared + shared; σ_2) errors. Ratio A is Model Aσ_1/Model Bσ_1 because both models were run using unshared-only errors. Ratio B is Model Aσ_2/Model Cσ_2 because Model C was run using the full error term. S.e.m is the standard error on the mean.

Boundary	MODEL A			MODEL B				MODEL C		
	Mean ± 2σ age	Error (%)		Mean ± 2σ age	Error (%)		Ratio A	Mean ± 2σ age	Error (%)	Ratio B
	(ka)	σ_1	σ_2	(ka)	σ_1	σ_2	A σ_1/B σ_1	(ka)	σ_2	A σ_2/C σ_2
End RBSR North	51.6 ± 4.2	8.1	9.6	51.6 ± 4.1	7.9	9.5	1.018	51.7 ± 4.4	8.6	1.121
RBSR South/RBSR North	56.4 ± 2.8	5.0	7.2	56.4 ± 2.8	4.9	7.2	1.014	56.4 ± 3.0	5.3	1.352
BBCSR/RBSR South	59.7 ± 2.3	3.9	6.5	59.7 ± 2.3	3.9	6.5	1.000	59.9 ± 2.5	4.2	1.562
BAS/BBCSR	64.5 ± 3.2	5.0	7.2	64.5 ± 3.3	5.0	7.2	0.995	64.6 ± 3.3	5.1	1.425
OBS2/BAS	68.4 ± 1.9	2.8	5.9	68.4 ± 1.9	2.8	5.9	0.994	68.3 ± 2.1	3.1	1.915
SGS/OBS2	70.2 ± 2.0	2.8	5.9	70.2 ± 2.1	2.9	6.0	0.952	70.0 ± 2.1	3.0	1.972
OBS1/SGS	71.8 ± 1.5	2.1	5.6	72.1 ± 1.7	2.4	5.7	0.881	71.7 ± 1.7	2.4	2.358
SADBS Upper/OBS1	72.7 ± 1.4	1.9	5.5	73.4 ± 1.7	2.3	5.7	0.808	72.8 ± 1.6	2.2	2.481
SADBS Lower/SADBS Upper	73.5 ± 1.3	1.7	5.5	74.4 ± 1.6	2.1	5.6	0.822	73.7 ± 1.6	2.2	2.491
ALBS/SADBS Lower	74.2 ± 1.5	2.0	5.6	75.6 ± 2.0	2.6	5.8	0.773	74.7 ± 1.9	2.6	2.186
CRS/ALBS	78.6 ± 3.2	4.0	6.6	78.9 ± 2.8	3.5	6.3	1.143	77.9 ± 3.7	4.7	1.403
LBSR Upper/CRS	81.1 ± 3.0	3.7	6.4	81.1 ± 2.9	3.6	6.3	1.023	80.9 ± 3.5	4.3	1.496
LBSR Lower/LBSR Upper	86.2 ± 2.6	3.0	6.0	86.2 ± 2.6	3.0	6.0	0.991	86.2 ± 2.8	3.3	1.838
YBSR/LBSR Lower	89.0 ± 2.9	3.3	6.2	89.0 ± 2.9	3.3	6.1	1.011	89.3 ± 3.2	3.6	1.732
YBS/YBSR	98.6 ± 6.5	6.6	8.4	98.7 ± 6.5	6.6	8.4	1.004	98.1 ± 6.4	6.5	1.286
BYS/YBS	103.8 ± 5.9	5.7	7.7	103.9 ± 6.0	5.7	7.7	0.997	103.3 ± 6.3	6.1	1.276
MBS	109.0 ± 9.4	7.3	9.0	108.0 ± 8.9	8.3	9.8	0.885	106.4 ± 9.9	9.3	0.967
						mean	***0.959***			***1.687***
						s.e.m	***0.025***			***0.108***
						median	***0.995***			***1.562***

Table 3
Summary of correlations between PP5-6 sequence and other proxies.

StratAgg	Age (ka)	MIS	Sediment type[a]	StratAgg thickness (m)[b]	Sea-level		Distance to coast	Speleothems	
					Direction	range (m BSL)	range (km)	$\delta^{13}C$ range	$\delta^{18}O$ winter rainfall
RBSR North	56.4–51.6	3	AS-P	0.15 (2.75)	regressive	57–68	12.4–7.6	C3 dominant	stronger
RBSR South	59.7–56.4	4	AS-P	0.9	regressive-transgressive	53–57	7.6–9.4	C3 dominant	stronger
BBCSR	64.5–59.7	4	RS	1.07	transgressive	81–53	9.4–24.7	C4 common	weaker
BAS	68.4–64.5	4 (peak)	AS	0.99	regressive	78–85	24.7–29.6	C3-C4 instability	unstable
OBS2	70.2–68.4	4	AS	1.78	regressive	73–78	24.7–18.7	C4 common	weaker
SGS	71.8–70.2	4	AS	0.53	regressive	70–73	13.2–18.7	C4 common	stronger
OBS1	72.7–71.8	5a-4	AS	0.67	regressive	64–70	10.6–13.2	C4 common	stronger
SADBS Upper	73.5–72.7	5a	AS	0.66	regressive	47–64	5.9–10.6	C4 common	stronger
SADBS Lower	74.2–73.5	5a	AS	0.37	regressive	44–47	2.8–5.9	C4 common	weaker
ALBS	78.6–74.2	5a	AS	1.43	regressive	25–44	1.2–2.8	C3 dominant	weaker
CRS	81.1–78.6	5a (peak)	E	0.37	stable-regressive	19–25	0.5–1.2	C3 dominant	weaker
LBSR Upper	86.2–81.1	5b-5a	RF	1.13	transgressive	42–19	0.5–2.4	C3 dominant	stronger
LBSR Lower	89.0–86.2	5b (peak)	RF	4.04	transgressive	48–42	3.7–2.4	C3 dominant	stronger
YBSR	98.6–89.0	5c-5b	RF-AS	1.07	transgressive-regressive	26–48	1.2–3.7	C3 dominant	stronger
YBS	103.8–98.6	5c	AS	0.54 (4.5)	transgressive-regressive	27–21	1.2–0.5	C3 dominant	stronger
MBS	109.0–103.8	5d (peak)	RF		transgressive	45–27	2.9–1.2	C4 common	stronger

[a] Sediment types refer to aeolian sand-dominated (AS), aeolian sand and palaeosol (AS-P), roospall-dominated (RS) and erosion (E).
[b] Thicknesses outside brackets represent average excavated maximum thickness and those inside brackets estimated unexcavated maximum thickness.

The 6 prior OSL ages for Conrad Sand are self-consistent ($P > 0.99$) and individually consistent with the $^{40}Ar/^{39}Ar$ age at 1σ. Their weighted mean OSL age is 75.5 ± (3.4, 5.2) ka at 95.4% probability, which is ~2.2% older than the YTT age and with σ_1 and σ_2 errors more than 5- and 8-fold larger than the YTT age uncertainty. Including the YTT in Model A does not significantly change the mean *End Boundary* posterior age for Conrad Sand at 95.4% probability (75.6 ka) compared to Model B, and none of the posterior ages are inconsistent with their prior ages. The greatest effects of including the YTT in Model A are: (1) to draw the posterior OSL ages slightly closer to the YTT age, resulting in slightly positively skewed probability density functions (left-hand panel in Fig. 11), and (2) to reduce the size of the individual age uncertainties (σ_1) to ~2.8% at 95.4% probability, or about half the size of their prior estimates.

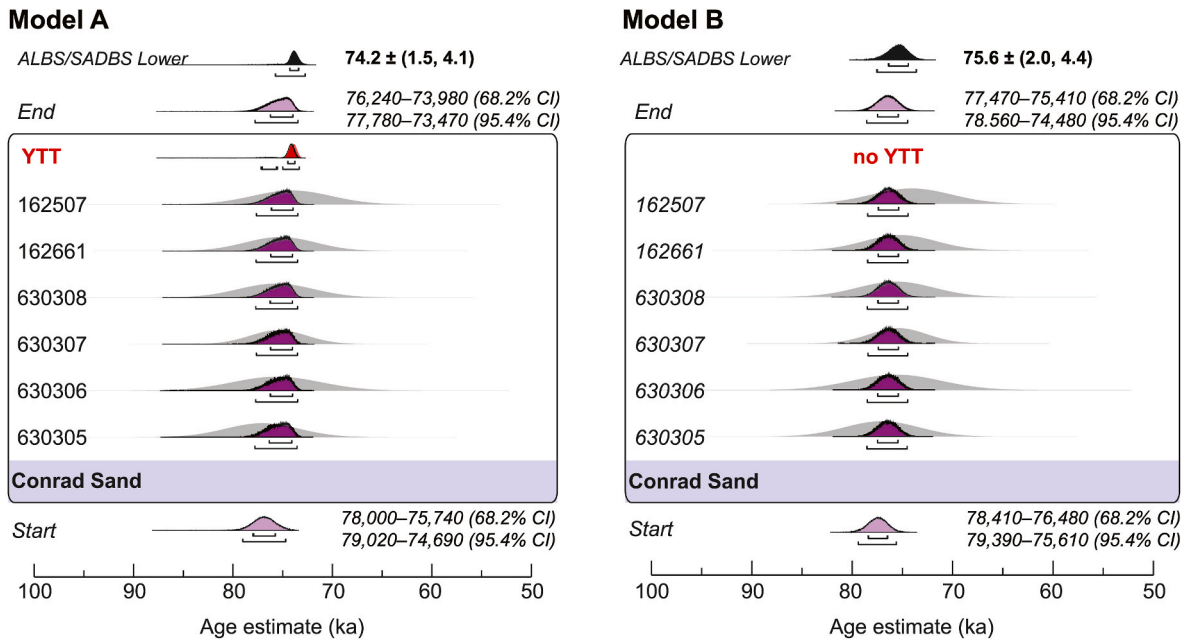

Fig. 11. Comparison of modelled ages for Conrad Sand treated as a '*Phase*' within ALBS. The precise $^{40}Ar/^{39}Ar$ age for the YTT is included in Model A and excluded from Model B. The posterior age ranges in calendar years are provided for the start and end of the Conrad Sand Phase. The mean ± (σ_1, σ_2) age for Transitional Boundary ALBS/SADBS Lower are given at 95.4% probability in ka.

Excluding the YTT age in Model B gives rise to normal probability distributions (right-hand panel in Fig. 11) with a mean *End Boundary* posterior age estimate of 76.5 ka, which is ~3.5% older than the YTT age. The uncertainties are smaller than those in Model A (by ~4.5% at 95.4% probability, respectively), which indicates that the inclusion of the YTT in Model A is not the sole driver of the significantly reduced σ_1 errors. The net effect of excluding the YTT age in Model B is that the *End Boundary* age for Conrad Sand is ~1.2% older than the age obtained by Model A, which is consistent with the YTT age at 95.4% probability.

The largest effect of including the YTT age is expressed in the *Transitional Boundary* estimate for ALBS/SADBS Lower (shown in black at the top of both panels in Fig. 11), which has a σ_1 uncertainty ~23% smaller in Model A than in Model B. Incorporating the YTT age as a tie-point in Model A, therefore, improves the overall accuracy and precision of individual modelled ages and posterior boundary age estimates for Conrad Sand.

4.5.2. Overall effect of including the YTT age in Model A

We also compared the mean ages of the modelled 95.4% probability distributions and their σ_1 errors for all 17 modelled boundary age estimates obtained using Models A and B; the ratios of their σ_1 errors are listed in Table 2 (Ratio A). The age estimates for the 17 boundaries are, on average, indistinguishable for Models A and B (mean ratio 0.992 ± 0.005, median 0.998), and their precisions are likewise consistent with an average ratio of unity (mean 0.959 ± 0.025, median of 0.995). Some of the precisions are higher in Model A (by about 23%, 18%, 19% and 12% for the age estimates of *Transitions ALBS/SADBS Lower*, *SADBS Lower/SADBS Upper*, *SADBS Upper/OBS1* and *OBS1/SGS*, respectively), but lower for *Transition CRS/ALBS* (by ~14%). A further 10 boundary ages have σ_1 errors for Models A and B within 2% of a ratio of unity, so the precisions are, overall, mostly unaffected by the inclusion of the YTT age as a tie-point and shows that the final ages are not critically sensitive to its inclusion or exclusion in the Bayesian model. Including the YTT age, however, improves the precisions of the boundary age estimates in the 75–72 ka interval.

4.5.3. Effect of including shared errors for individual ages in the model

The uncertainties associated with OSL ages consist of a combination of random and systematic errors, many of which are shared between individual ages. The systematic components of error arise when all measurements are affected in the same way, resulting in a systematic bias in each of the measurements. The type and size of the errors will vary between laboratories and even between studies conducted at the same laboratory. We estimate the mean relative shared error for the OSL samples in this study to be 2.58% at 1σ, or 5.16% at 2σ, which amounts to ~44% of the total uncertainty (i.e., σ_2 error) for our samples.

The key issue with systematic errors (all shared) is that they cannot be reduced in size by increasing the number of measurements or the number of model iterations, so they effectively control the lower limit of precision achievable for OSL ages (e.g., Rhodes et al., 2003; Wood et al., 2016; Jacobs et al., 2019). If the shared and unshared errors are not treated separately when combining ages, especially for a large dataset collected and analysed in a systematic way, then the final modelled uncertainties can greatly underestimate the true uncertainties (i.e., the σ_2 errors will be too small if the shared errors are also reduced in size).

To evaluate the impact of incorporating shared errors on the accuracy and precision of the modelled age results, we compared the results obtained from Models A and C. The latter model is applied to the ages and their σ_2 errors, rather than their σ_1 errors, so the shared errors are also (incorrectly) reduced in size. In Table 2, the mean ages of the posterior 95.4% probability distributions and the σ_2 errors estimated by Model C are listed for the 17 boundary ages, together with the ratios of the σ_2 errors for Models A and C (Ratio B). For all 17 boundary estimates, Model C underestimates the σ_2 errors, on average, by 70 ± 11% (median 56%). The individual discrepancies range from as little as 3% for the oldest boundary age (*Start PP5-6S*) and 12% for the youngest boundary age (*End RBSR North*) to more than two-fold for *Transition ALBS/SADBS Lower*, *SADBS Lower/SADBS Upper, SADBS Upper/OBS1* and *OBS1/SGS*. With the sole exception of *Start PP5-6S*, the underestimation is systematic across the board and the magnitude of underestimation is greatest for boundary ages with the smallest σ_1 errors. The total relative uncertainties (σ_2 errors) on the modelled boundary ages of 2.2–2.6% at 2σ are not credible, as they are smaller than the known size of the sum of shared errors (relative error of 5.16% at 2σ). This comparison underscores the need to remove the shared errors associated with OSL ages before combining them, whether in a Bayesian model such as this or in

an alternative model (e.g., Jacobs et al., 2008a), especially for ages that have σ_1 errors estimated with high precision.

4.6. StratAgg-specific results

The results presented in sections 4.1–4.5 discuss average patterns and trends. To allow for closer scrutiny of the data, results are also presented separately for each StratAgg in Section 3 of Supplementary Information. The information is summarised in a separate composite figure for each StratAgg (Figs. S1–S13) using the same colour scheme as in Fig. 2. The data for SADBS is shown in Fig. 12 as an example; see caption and Section 3 in Supplementary Information for details. Panel E in each of the StratAgg-specific figures shows the relevant portion of the full Bayesian age model output following the same format as in Table S5. The age scale (160–40 ka) are the same for each StratAgg to facilitate comparison between StratAggs. Creating a single continuous figure that include all data on a single page is not feasible.

Each figure is also supplemented by summary text, including a short description of the StratAgg, a list of SubAggs sampled and dated, discussion of any patterns in D_e, dose rate and individual measured ages, together with the specific modelled boundary age estimates and duration of the StratAgg.

4.7. Ages from 'other' contexts

Age estimates for 28 samples from various 'other' contexts, not included in the Bayesian age model, are listed in Table S2 according to context type: (1) dunes, (2) PP5-6S sheetwash and gully fill, (3) debris flows (StratAggs BCS and DBCS; Fig. 2) including a remnant of cemented colluvium sampled from the rockshelter wall of PP5-6N, and (4) cut-and-fill features (upper and lower) (Fig. S14). The dune samples were collected to determine the timing of dune deposition around the site in the absence of anthropogenic impacts and for comparison to the timing of the aeolian sand (AS)-dominated StratAggs in PP5-6 (Fig. 10). The other types indicate different processes that modified the site and are divided in this way for ease of discussion. The three packages are not mutually exclusive; cut-and-fill features also contain sheetwash and debris flows. Sampling was not comprehensive, and the aim was not to reconstruct all known erosional events. The main purpose was to see whether we could use single-grain OSL dating as a tracer of sediment movement to pinpoint major and minor erosive events.

The ages and their σ_1 uncertainties for all samples are displayed as probability density distributions (PDF) in Fig. 13A–D. PDFs for samples where CAM (Fig. 7A) or nMAD CAM (Fig. 7B) was used to determine D_e are shown in black. When FMM (Fig. 7C) was used the PDF for each component is shown in shades of grey weighted according to the proportion of grains that make up each component (shown in Table S2).

The ages for the dune samples fall into two clusters (Fig. 13A): one sample (142624) dated to 99 ± 5 ka consistent with YBS, and four samples ranging in age from 74 ± 5 to 67 ± 4 ka consistent in age with ALBS–BAS. The dunes outside the cave, therefore, show good consistency with all AS-dominated StratAggs, except RBSR North (Fig. 10).

We next used the FMM to determine whether ages for different samples cluster. Some samples have multiple age components, so each age was input separately for a total of 40 age estimates (Table S2). We used the weighted mean ages and their respective σ_1 errors and assumed zero overdispersion for each age component. We treated the Holocene (blue; Fig. 13E (n = 17)) and Pleistocene (red; Fig. 13F (n = 23)) ages separately. For each dataset four discrete age clusters were determined; stippled blue and red lines are centered on the weighted mean age of each cluster. We did not include the ages for the dune samples in this calculation, but they are shown as open squares in Fig. 13F. We also did not include any modern age components; for some samples this component is significant (see Table S2). The weighted mean age for each cluster (labelled a–h) and its 2σ error are also indicated as red and blue vertical bars in Fig. 13B–D, G.

The 8 age clusters (shown as a–h in Fig. 13) can be divided into two parts: three clusters (a–c) that pre-date 50 ka during the active phase of site formation and occupation, and five clusters (d–h) that post-date 50 ka.

Almost all of the samples (11 of 14) that pre-date 50 ka have single component D_e distributions, including all samples from DBCS and BCS; nMAD CAM was used as only very few grains were identified as outliers and were randomly distributed (Table S2). The other three samples had two or more discrete dose components, but with a major dose component represented by 80% (162760), 87% (571369) and 89% (162753) of grains.

'Cluster-a' (92 ± 5 ka) is consistent with YBSR. This is represented by a single sample from Lower CAFF and represents its original depositional age with the minor component reflecting the disturbance. Cluster-a does not represent an erosive event.

'Cluster-b' (69 ± 2 ka) has ages consistent with the period from the start of OBS1 to the end of BAS. These samples are found in three different areas: (1) three samples from DBCS, the southernmost sampled debris flow (Fig. S15), (2) three samples from Upper CAFF, and (3) two samples from Lower CAFF. The latter samples were collected as 'balls' of dark sediment found within a disturbed sandy matrix at the bottom of the sequence, representing eroded remnants of deposit that derive from much higher up in the sequence. The age correlations with OBS1–BAS and the D_e distributions that show little evidence for mixing, suggest that sediment likely moved on mass without re-exposing the grains to light. The age of the deposit could, therefore, be the age of the unit from which it is derived, and the minimum age (61 ± 2 ka) of this distribution of ages could represent the maximum possible time of the debris flow event. This would coincide with the BBCSR, a roof-spall dominated unit characterized by debris flows signifying a period of site instability.

'Cluster-c' (57 ± 1 ka) has ages consistent with the start of RBSR South to the transition with RBSR North (Fig. 10) and includes two ages from BCS (Fig. S15) as well as samples from the Upper and Lower CAFF. The character of RBSR South and SubAgg Ellis at the base of RBSR North are consistent with being debris flows. Cluster-c is also consistent with the age of the cemented colluvium collected from the rockshelter wall (142625). So, this cluster could represent an erosive event that impacted the entire site.

Clusters d–h all post-date 50 ka and, therefore, must represent a series of erosive events. All clusters, except cluster-g have at least two samples where the age of the cluster is the major age component for that sample. 'Cluster-g' (524 ± 66 years) only occurs in very small proportions (1.5–8%) in four samples from Upper CAFF and is not considered significant. 'Cluster-d' (41 ± 1 ka) is a dominant age component in one sample from BCS and two samples from Upper CAFF and occur as more minor but significant components (16–42%) in a further five samples from Upper and Lower CAFF. 'Cluster-e' (7.7 ± 0.2 ka) is represented by two samples, one from sheetwash deposits inside PP5-6S (571343; StratAgg CLS) and the other (110598) from fill in an erosion gully immediately in front of PP5-6S. These two samples may date the re-opening of PP5-6S after it was choked and blocked by Pleistocene dune sands before ~100 ka ago (Table S1). This age cluster is also represented in two other samples from Upper and Lower CAFF, but with very small proportions of grains (2–5%). 'Cluster-f' (1.84 ± 0.08 ka) is represented by the major age components in two samples from Lower CAFF and 'cluster-h' (204 ± 18 years) by two samples from Upper CAFF.

Together, three major erosional events (clusters b, c and d) had site-wide impacts and three minor erosional events (clusters e, f and h) more localized impacts.

4.8. Timeline for the sedimentary sequence and human occupation of PP5-6 for comparisons with other sites and proxies

We used the mean modelled boundary age estimates for StratAggs in Fig. 10 to create a common time scale from 110 to 50 ka (MIS 5d–3; Lisiecki and Raymo, 2005) (Fig. 14A) for the sedimentary sequence from

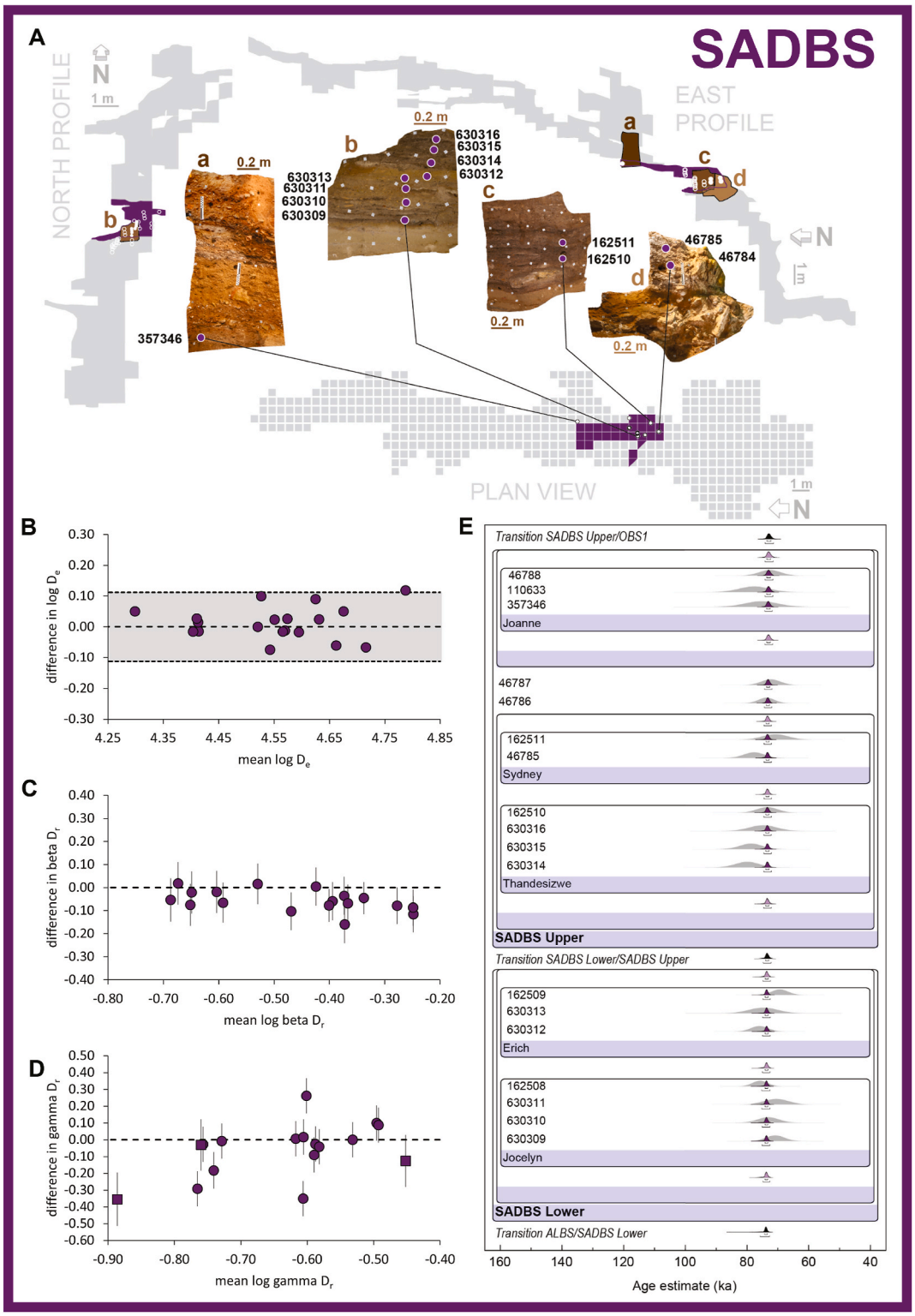

Fig. 12. Composite figure containing information about sample locations, OSL dating results and the specific part of the full Bayesian age model for StratAgg SADBS. **A**, Location of SADBS in cross-sectional and plan views of the site, photographs of the key stratigraphic profiles from which samples were collected, and thumbnails on the cross-sectional profile. OSL sample positions are marked on the plan view, photographs and thumbnails with corresponding sample codes listed next to the profiles. **B–D**, Differences between each pair of log D_e (**B**), log beta D_r (**C**) and log gamma D_r (**D**) as an Oldham plot (see Section 4). **E**, Relevant portion of the full Bayesian age model output following the same format as in Table S5. The age likelihood distributions (prior to modelling) are shaded grey, and the posterior (mathematically modelled) distributions are coloured. SubAggs with more than one age estimate are shown in a box with the SubAgg name in the associated blue bar, and boundary ages between SubAggs are shown as probability distributions in pale colours. Start, Transitional and End Boundaries are shown as black probability distributions. The narrow and wide brackets beneath each distribution represent the 68.2% and 95.4% probability ranges, respectively. (For interpretation of the references to colour in this figure legend, the reader is referred to the Web version of this article.)

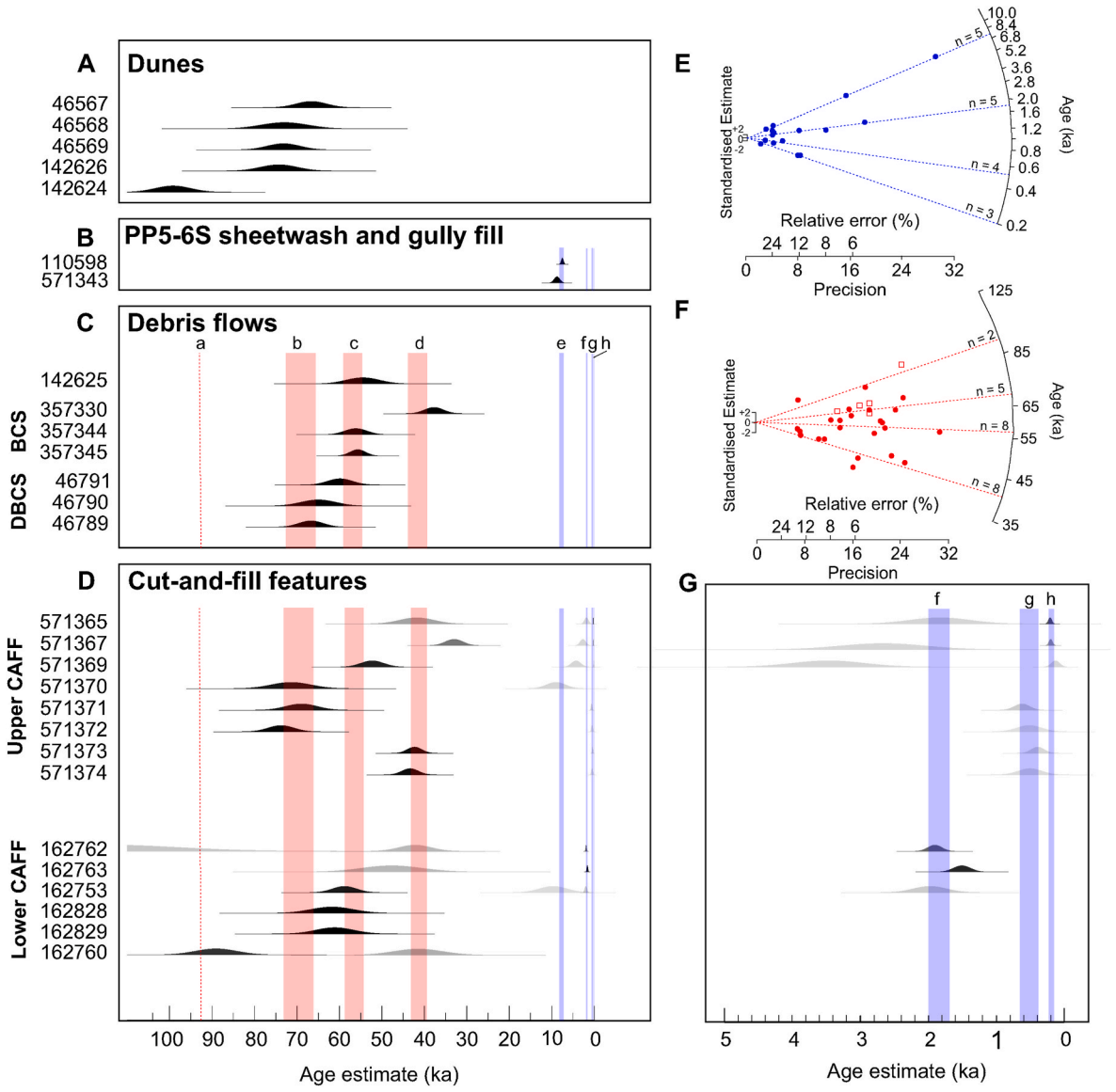

Fig. 13. **A–D**, OSL ages for 28 samples from different contexts. Ages are shown as probability density distributions; black where CAM or nMAD CAM was used to determine D_e and shades of grey where FMM was used, adjusted based on proportion of grains included in the age component. Vertical bars are the weighted mean age estimates and 2σ errors for eight age clusters (a–h) determined using the FMM for **E**, Holocene ages (blue; n = 17) and **F**, Pleistocene (red; n = 23) ages shown as filled circles. Ages for 4 dune sample are also shown as open squares in **F**. **G**, shows the same data as **D**, but for only the last five thousand years. (For interpretation of the references to colour in this figure legend, the reader is referred to the Web version of this article.)

PP5-6 (Fig. 14B). Here and in the discussion, we use the mid-point ages, but with the knowledge that each estimate has uncertainties provided fully in the relevant data tables (Tables S1, S2 and S5).

For interpretation of the sedimentary record, we show in Fig. 14C the timing of four types of records: (1) general character of the sediments in each StratAgg; aeolian sand (AS)-dominated, roofspall (RS)-dominated or both, (2) dunes in and around PP5-6 (Fig. 13A), (3) StratAggs that contain significant debris flows including DBCS (light blue) and BCS (light green) not included in the age model, and OBS1, BBCSR and RBSR South (vertical grey lines), and (4) ages for Pleistocene erosional events (cluster-b and cluster-c in Fig. 13C and D).

For interpretation of the archaeological record, we show in Fig. 14D any significant breaks (hiati) in occupation and three types of occupation. We also summarise from Brown et al. (2012) and Wilkins et al. (2017) the dominant raw materials and tool types.

StratAggs by their very definition group layers that are bounded by major erosional unconformities or depositional discontinuities (Karkanas et al., 2015). Throughout the sequence there are contacts with evidence of transitional boundaries, as well as boundaries indicative of discontinuous sedimentation (i.e., erosional contacts). This includes, for example, decalcified erosional interfaces between adjoining StratAggs (e.g., SADBS and OBS1 and SGS and OBS2) and thin layers of pure roofspall or sandy-roofspall deposited through natural processes devoid of archaeological finds (e.g., throughout YBSR and LBSR) (Karkanas et al., 2015). Many of these discontinuities are at a temporal resolution that cannot be resolved with OSL dating. So, for the age model, we assumed that the sediment deposition was continuous, or nearly so (see Section 2 in Supplementary Information). Here we only refer to three types of breaks in occupation: (1) entire StratAggs devoid of archaeological finds (e.g., YBS and BYS), (2) StratAgg CRS that represents an unconformity between LBSR and ALBS, associated with the weathering and exposure of the LBSR, and (3) intra StratAgg breaks associated with aeolian sands whose ages were directly estimated and modelled and that are separated by thick layers of occupation (e.g., OBS2; RBSR North). We also scrutinized the ages around each of the transitional boundaries in the age model (Table S5) and found that there is a gap in ages between

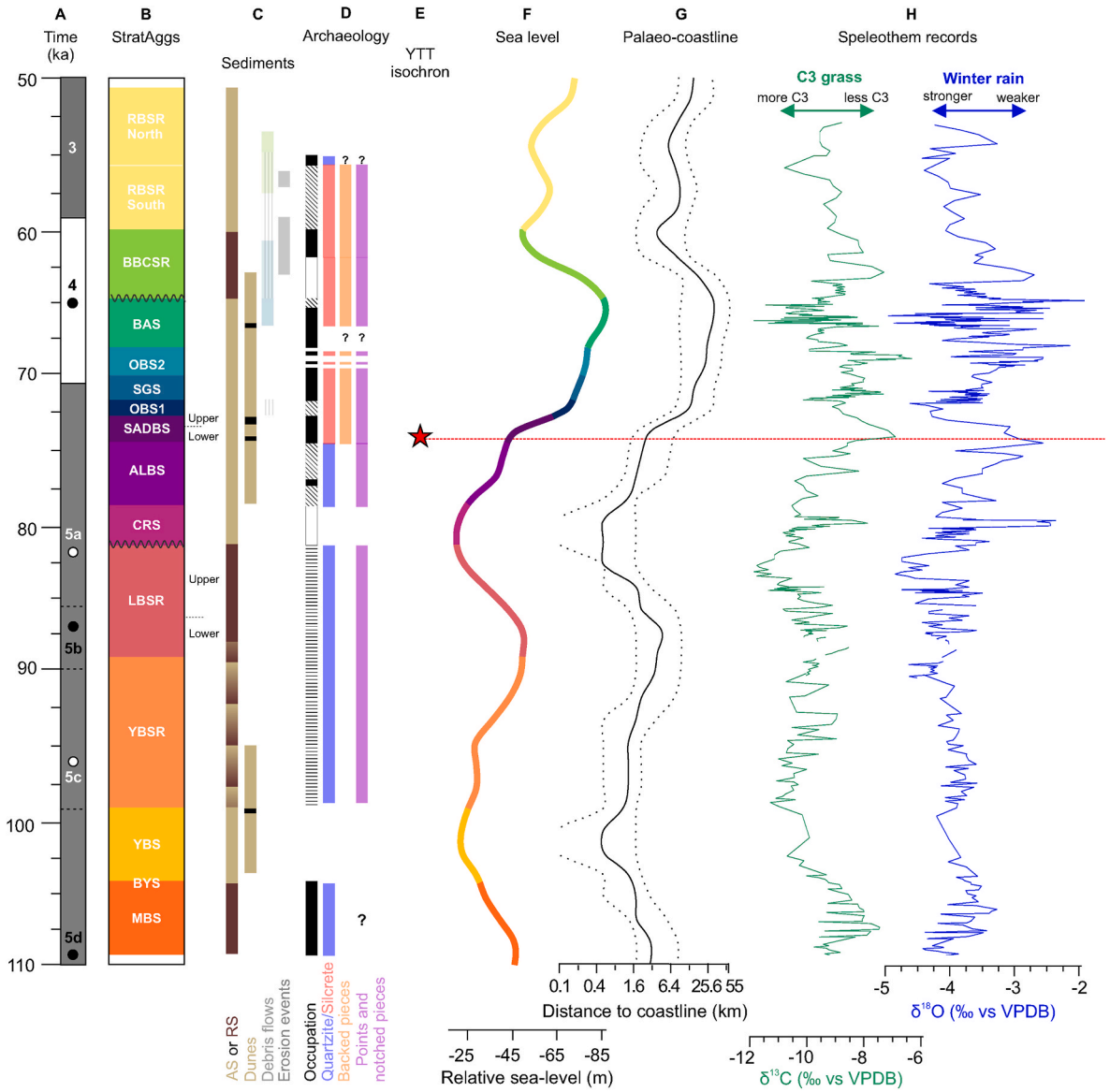

Fig. 14. Timeline of Stratigraphic Aggregates and sediment deposition at PP5-6 and changes in sea level, vegetation, and rainfall in the immediate area. **A,** Timescale from 110 to 50 ka together with MIS stages and sub-stages. The peak of each stage/sub-stage is indicated by a filled circle (white for interglacial/interstadial and black for glacial/stadial). **B,** Individual StratAggs positioned along the timeline using the colour legend in Fig. 2 and the mean ages for each start, transitional and end boundary in Fig. 10. The stippled lines to the right of LBSR and SADBS indicate the timing of transition from the informal Lower to Upper subdivisions in these two StratAggs and the wavy lines indicate two erosional unconformities. **C,** First vertical bar indicate whether a StratAgg is aeolian sand (AS-; light brown) or roofspall (RS-; dark brown) dominated or both. Second vertical bar indicate timing of two dune pulses in and outside PP5-6 (Table S2; Fig. 13); the black horizontal bars denote the mean age for each of the five dune samples in Table S2 and the vertical bars represents their 1σ uncertainties. Third vertical bar shows the timing of significant debris flows, DBCS (light blue), BCS (light green) and in OBS1, BBCSR and RBSR (vertical grey lines). Fourth vertical bar shows timing of two Pleistocene periods of erosion and site disturbance; minimum age for cluster-b, cluster-c and cluster d in Fig. 13. **D,** Archaeological record of PP5-6. First vertical bar shows breaks (white) and three different types of occupation (dense (black), discrete (horizonal lines) and episodic (diagonal lines). Second vertical bar shows the dominant raw material (red, silcrete and blue, quartz). Third vertical bar shows the presence of backed pieces (orange), and fourth bar the presence of points, notched pieces and pièces esquilées (purple). **E,** Red star positions the Toba isochron on this time axis. It is shown at its correct age of 73.88 ka, which is within error of its position near the top of ALBS (Fig. 11). **F,** Glacio-eustatic sea-level curve of Waelbroeck et al. (2002). Different colours correspond to different StratAggs in **B**, **G,** Mean (solid line), minimum and maximum (stippled lines) distance to modern coastline in km using the data provided in Fisher et al. (2010). The curve is shown on a logarithmic scale with 55 km the maximum distance. **F,** $\delta^{13}C$ (green) and $\delta^{18}O$ (blue) stable isotope values shown using the PP29 speleothem record from 110 to 90.5 ka (Braun et al., 2019) and the Crevice Cave record from 90.5 to 53 ka (Bar Matthews et al., 2010). (For interpretation of the references to colour in this figure legend, the reader is referred to the Web version of this article.)

the top of BAS and the bottom of BBCSR, associated with the larger uncertainty of the BAS/BBCSR modelled boundary age estimate (Fig. 10). We infer that the difference in age between the boundary age and the start of occupation in BBCSR is also a break, consistent with the observed sediment disconformity between these two StratAggs. These are shown together with the other breaks as white bars in Fig. 14D.

Occupation also presents in different ways. Here we divided it into three types: (1) discrete (horizontal lines), (2) episodic (diagonal lines) and dense (black). Discrete refers to StratAggs with individual intact lenses of shell and burnt sediment alternating with sterile roofspall or sandy layers in YBSR, LBSR and OBS2. Karkanas et al. (2015) interpreted these occupations as representing low intensity, but high frequency

short visits. Episodic refers to aeolian-dominated StratAggs with thin lenses of occupation holding few finds in ALBS, OBS1, the top of BAS in SubAgg Achilles and throughout RBSR South. Karkanas et al. (2015) interpreted these occupations as representing low intensity, low frequency short visits. Dense denotes StratAggs made up of thick accumulations (palimpsests) of hearth features that were trampled and/or reworked (SADBS, SGS, BBCSR, BAS and SubAgg Ellis in RBSR North) as well as those with more finely bedded layers, within an aeolian environment, rich in finds (Conrad shell in ALBS). Karkanas et al. (2015) interpreted these occupations as high intensity, high frequency short visits.

Placement of the sedimentary and archaeological records on a common timescale then allows for direct comparison to four key records (Fig. 14E–H): (1) the Toba isochron found in PP5-6N (Smith et al., 2018), (2) the glacio-eustatic sea-level curve (Waelbroeck et al., 2002), (3) changes in the distance to coastline due to exposure of the Palaeo-Agulhas Plain during lower sea-levels modelled for Pinnacle Point (Fisher et al., 2010) and, (4) the $\delta^{13}C$ and $\delta^{18}O$ stable isotope records from speleothems in Crevice Cave and PP29 (Bar Matthews et al., 2010; Braun et al., 2019).

5. Discussion

5.1. Chronological resolution

In this study, we dated 197 samples using single-grain OSL dating with the main purpose to reduce uncertainties and increase chronological resolution. Individual OSL ages are typically associated with large uncertainties (>5%), because they are made up of many separate measurements to obtain estimates of D_e and dose rate, each with its own set of systematic and random uncertainties. For samples from PP5-6 the median total relative error (σ_2 error) is 5.9%. At 50 and 110 ka (the age range for samples from PP5-6), this represents 2950 and 6490 years at 1σ, respectively or about 102 or 224 human generations, assuming that each generation is 29 years (Fenner, 2005). This is too coarse to truly understand, on human timescales, behavioural and cultural processes, the impacts of demographic changes on resident populations and short-term environmental variations on resource use.

PP5-6 afforded a unique opportunity to improve the resolution of the chronology. The site is finely-stratified, and stratigraphic and archaeological information are collected at high resolution. Intensive fieldwork alongside archaeologists and geoarchaeologists over almost two decades allowed collection of sediment samples with high stratigraphic integrity and spatial control, and contextual support for use in interpretation of the OSL data. OSL samples were collected from individual SubAggs and multiple samples from the full vertical extent of each StratAgg. Direct measurement of the gamma dose rates for each sample was prioritised. OSL measurements and data analysis were done in a systematic and reproducible manner and numerous sensitivity tests and comparisons conducted to identify problems and create solutions, providing confidence in the quality and reliability of the data. This systematic approach allowed several of the largest uncertainties attached to OSL ages to be removed when comparing ages against each other. That is, the systematic or shared error terms (~44% of the total uncertainty for our samples) will be the same for each age, so it will not affect comparisons between estimates; only the random (unshared) measurement errors listed as σ_1 values in Tables S1 and S2 will contribute to uncertainty in age. This is also the error most suitable for use in age modelling.

Individual OSL ages are also rarely of direct interest to the archaeologist. Statistical approaches, such as Bayesian age modelling, offer opportunities to combine multiple ages, model boundary estimates and answer specific questions. Such models consider the ages and their σ_1 uncertainties together with the high-resolution stratigraphic and archaeological data that are used as prior information to structure the model. Because samples were collected from individual SubAggs for which the arrangement is well established, all ages could then be modelled in strict sequence, outliers can be detected and their ages down-weighted in the model. The many age estimates for each StratAgg, use of σ_1 uncertainties and knowing the strict stratigraphic sequence of each sample together allows for optimization of precision and construction of a high-resolution chronology. In this context, dating of more samples with high stratigraphic integrity is better.

This approach resulted in a chrono-stratigraphic model for PP5-6 (Fig. 10). The accuracy of the model was demonstrated by comparison and also inclusion of the high-precision $^{40}Ar/^{39}Ar$ age for the YTT in ALBS. Uncertainties for individual boundaries vary. Those at the top and bottom of the sequence are least precise (~4% at 1σ for σ_1 errors) and those in the middle most precise (<1% at 1σ). The latter is a consequence of the inclusion of the $^{40}Ar/^{39}Ar$ age for the YTT, and the relatively small differences in age and short durations of contiguous StratAggs. The age model allowed us to create a common timeline for sediment deposition and human occupation of PP5-6 (Fig. 14) that is bringing us much closer to the required temporal resolution to look for finer-grained patterns within the PP5-6 record and seek correlations with other proxies to better understand the temporal changes in site formation and occupation at PP5-6.

The ages presented in this paper and the resulting Bayesian age model now supersedes all previously published ages for PP5-6 (Brown et al., 2009, 2012; Smith et al., 2018) and general use of ages in other manuscripts (e.g., Karkanas et al., 2015; Wilkins et al., 2017; Cawthra et al., 2020; Esteban et al., 2020b; Matthews et al., 2020). Some adjustments are required for the timing of major cultural events such as intensification in use of silcrete and heat treatment and the start of microlithic technology. Below we provide a refined interpretation and discussion of the PP5-6 sedimentary and archaeological records using the common timeline presented in Fig. 14.

5.2. The PP5-6 sedimentary record

Table 3 provides a summary of key correlations for the sediments in each StratAgg and other records. Sediment deposition appears to be closely linked to changes in global sea-level and climate (Fig. 14A–F) with many of the StratAggs, and changes from one to the other, coinciding with major global climatic events. The base of the sequence in MBS coincides with the peak of sub-stage MIS 5d. YBSR spans the entire sub-stage MIS 5c. LBSR Lower spans sub-stage 5b. The transition from LBSR Lower to LBSR Upper occurs at the transition from MIS 5b to MIS 5a and LBSR Upper accrued during the period leading up to the peak of sub-stage MIS 5a. CRS to SGS spans the period from the peak to the end of MIS 5a. OBS2 to BBCSR all fall within MIS 4. RBSR South coincides with the start of MIS 3, dated in the Southern Hemisphere to ~59 ka (De Deckker et al., 2019).

AS-dominated StratAggs accumulated during sea-level regressions (from 19 to 85 m BSL) and site to palaeo-coast distances of 0.5–30 km. RS-dominated StratAggs accumulated during sea-level transgressions (from 55 to 19 m BSL) and site to coast distances of 0.5–7.1 km. The key difference is, therefore, in the direction of sea-level change and RS-dominated sediments accrue only during sea-levels higher than ~55 m BSL. Two StratAggs deviate from this pattern—YBSR and RBSR. YBSR (and the bottom of LBSR Lower, below SubAgg Bruce Red) shows alternating contributions of AS and RS; sometimes there are more sand and other times more roofspall. Sea-level oscillations during MIS 5c are likely responsible for this alternating pattern. RBSR South and RBSR North are both predominantly made up of aeolian sand that were subsequently pedogenically altered. The coincidence of the deposition of these StratAggs with sea-level oscillations during MIS 3 may imply aeolian deposition during sea-level regression and pedogenesis during subsequent sea-level transgression.

There are no discernible chronological breaks in the depositional sequence, consistent with the near-continuous accumulation of sediment at the site, at least at timescales commensurate with the size of the age uncertainties. A major erosional unconformity is found at the top of

LBSR (shown as a wavy line in Fig. 14B). The unconformity is associated with surface erosion, roof collapse, cementation and gully formation (Karkanas et al., 2015). It corresponds with the peak of MIS 5a after a period of rapid sea-level transgression (~25 m from 42 to 19 m BSL in ~2.5 ka). Subsequent sediment deposition above this unconformity in CRS brackets the timing of this erosional event (81.1–78.6 ka). During CRS, sea-levels were consistently high (25–19 m BSL), the highest levels achieved during the period of sediment accumulation in PP5-6N (Fig. 14F), bringing the coast to within 500 m (minimum 80 m) of the site (Fig. 14G). CRS also overlaps with a significant increase in contribution from summer convective rains (Fig. 14H; see Bar-Matthews et al. (2010) and Braun et al. (2019) for interpretation of the Crevice Cave speleothem record here and elsewhere in the text). Another major erosional unconformity is found at the top of BAS. There is a gap between modelled ages found on either side of the transitional BAS/BBCSR boundary—SubAgg Achilles at the top of BAS ended at ~65 ka and SubAgg Nicol at the base of BBCSR started at ~62 ka (Table S5). The apparent continuity is an artefact of the model and use of a transitional boundary. This gap in sedimentation is consistent with field observations that the top of BAS has been eroded in parts of the excavation.

This unconformity at the top of BAS (shown as a wavy line in Fig. 14B) overlaps with the end of cluster-b (Fig. 13B and C) the first of three periods (clusters-b, -c and -d) of major site disturbance and sediment re-deposition during the Pleistocene associated with large-scale debris flows and cut-and fill features at the northern and southern ends of the site (grey bars in Fig. 14C). These include archaeologically-rich DBCS (light blue in Fig. 14C) and BCS (light green in Fig. 14C) and overlaps with BBCSR and RBSR that are both affected by gravity-flow processes (vertical grey bars in Fig. 14C). The onset of these events at ~62 ka coincides and follow a period of significant unstable climate leading up to the peak of MIS 4 in BAS, followed by a change from an increase in contribution from summer convective rains back to stronger winter stratiform rains during a period of rapid sea-level transgression (~30 m from 84 to 55 m BSL in ~2 ka; Fig. 14H; Table 3). Intense convective rains may have led to saturation of the sediments facilitating debris flows (Karkanas et al., 2015).

Together, these erosional events and CRS could explain the erosional profiles observed today. The evidence for large-scale erosion during the Holocene is elusive, although sea-levels were high enough to partially re-open PP5-6S at ~8 ka (Fig. 13B) and could have undermined and reworked deposits at the base of PP5-6N, for which there is also evidence at ~2 ka (Fig. 13G).

5.3. The PP5-6 archaeological record

Table S6 provides a summary of the timing of different types of human occupation (Fig. 14D) and key correlations with other records (Fig. 14E–H).

5.3.1. Changes in the pattern of human occupation

Human occupation of PP5-6 was punctuated and varied through time (Fig. 14D). First and last evidence of human occupation was in MBS in PP5-6S (109.0–103.8 ka) and the base of RBSR North in SubAgg Ellis (56.4–55.0 ka). The longest breaks in occupation are associated with YBS/BYS (103.9–98.5 ka), CRS (81.1–78.6), BAS/BBCSR transition (64.9–61.9 ka) and RBSR North after SubAgg Ellis (55.0–51.6 ka); the latter caps the whole sequence. Breaks in OBS2 that could be dated are typically short (~200–600 years).

Episodic occupation was represented by as few thin and less dense occupation lenses in two otherwise pristine dune sands in ALBS dated to 78.6–77.2 ka and 76.9–74.2 ka. It also occurs in OBS1 (72.7–71.8 ka) as lenses of trampled and reworked combustion feature palimpsests and shellfish remains, sometimes looking like debris flows (Fig. 14C) and in SubAgg Achilles at the top of BAS (65.3–64.9 ka) that contain only few finds. In RBSR South (59.7–51.6 ka) it manifests as thin lenses with few finds, mostly stone tools and bone (Brown et al., 2012) many of which also look like debris flows (Karkanas et al., 2015). The relative duration of these periodic occupations is unknown, except for Achilles that was directly dated.

Discrete occupation occurred mostly over longer periods of time (2.8–9.6 ka) when the main formation process was free-fall roofspall (Karkanas et al., 2015), sea-levels were transgressing and the coast was relatively close to the site (0.5–3.7 km). These are found mainly in YBSR (98.6–89.0 ka) and LBSR. LBSR Lower (89.0–86.2 ka) is like YBSR, just more heavily occupied (i.e., richer in finds), and LBSR Upper (86.2–81.1 ka) has higher frequencies of combustion features and finds.

Dense occupations occurred mostly over shorter periods of time (0.2–3.4 ka) when the main formation process was aeolian sand (Karkanas et al., 2015), sea-levels were regressing (36–84 m BSL) and the site was located further away from the coast (1.7–30 km). These are found mainly in ALBS Conrad Shell (77.2–76.9 ka), SADBS Lower (74.2–73.5 ka), SADBS Upper (73.5–72.7 ka) and SGS (71.8–70.2 ka), intermittently throughout OBS2 between 69.2 and 68.8 ka, and in BAS South (68.4–67.9 ka) and BAS North (67.9–65.3 ka). There is, however, one exception: MBS and BBCSR, the only two StratAggs with dense occupation that have sediments that are RS-dominated. Occupation during BBCSR (~62–59.7 ka) occurred like for other RS-dominated StratAggs when sea-levels were transgressing from 55 to 48 m BSL and the coast was nearer (7.1–3.6 km). MBS is from a cave (PP5-6S) rather than the rockshelter, so it may not preserve evidence in the same way.

5.3.2. Impacts of changing climates and environments on technology and raw material use through time

PP5-6 was used regardless of distance from coast (0.5–30 km). It was used while close to the coast (109–74.2 ka), some distance away with the Palaeo-Agulhas Plain exposed (74.2–72.7 and ~62.5–55.0 ka) but still within the typical 10 km daily foraging radius of hunter-gatherers (Marlowe, 2005), and when the sea was a long distance away (72.7–62.5 ka).

During the first ~35 ka (from 109 to 81.1 ka in MBS–LBSR Upper and 78.6–74.2 ka in ALBS), people would have experienced an environment and climate that was not too dissimilar to what we observe today. Sea-levels were above ~48 m BSL and the coast was near (<3.7 ka) with mixed sandy-rocky beaches common (see Cawthra et al., 2020 for interpretation of beach types). C3 vegetation was dominant, consistent with phytoliths (Esteban et al., 2020), and winter stratiform rains prevailed (Table S6). Quartzite was the dominant raw material type with moderate frequencies of silcrete and low frequencies of quartz and chert. There is a diverse range of tool types including points, notched pieces and *pièces esquilées* (Wilkins et al., 2017).

The first significant change occurred towards the end of ALBS in Conrad Sand and transition to SADBS Lower (76.9–73.5 ka), coincident with the Toba eruption (Fig. 14E). A stronger contribution from summer convective rains occurred, alongside a shift from C3-dominated vegetation to a more common occurrence of C4 plants and a change to longer sandy beaches. SADBS Lower (76.9–73.5 ka) and SADBS Upper (73.5–72.7 ka) were then associated with an acceleration in falling sea-levels (~20 m in ~1.5 ka) coupled with a shift again to stronger winter rainfall during SADBS Upper. This also coincides with the first appearance of microlithic technologies (Clark, 1985; Kuhn, 2002; Brown et al., 2012) and a shift from quartzite (still dominant in ALBS) to silcrete as the dominant raw material used for stone tool production, often in association with heat treatment (Brown et al., 2012). Relatively high frequencies of chert and quartz and a diverse range of tool types, including points, notched pieces and *pièces esquillées* continues from the preceding periods (Wilkins et al., 2017). Occupants of the site would have experienced the effects of sea-level change within their own lifetimes; ~40 cm fall in sea-level per generation, fastest during SADBS Upper. No other period during the occupation of PP5-6 achieved such rapid change (0–14.5 cm/generation, excluding episodic occupation in Nate/Leesha/Charles in ALBS; median = 7.3 cm/generation; Table S6).

OBS1 (72.7–71.8 ka), a short period characterised by episodic occupation, saw a shift back to C3-dominated vegetation and a period of relatively stable sea levels (68–70 m BSL) and a distance of ~12–13 km from the shore. Substantial amounts of shellfish remains are present. The stone tool assemblage contains few diagnostic tools, including two backed pieces near the boundary with SADBS, and an abundance of quartz (Brown et al., 2012).

The next significant change occurred during SGS (71.8–70.2 ka) at the transition from MIS 5a to MIS 4 with more of the Palaeo-Agulhas Plain being exposed (13–18 km from site to shore), opening up a landscape characterised by reflective pocket beaches, dunes, coastal lakes and wetlands (Cawthra et al., 2020) and winter rainfall still dominant. SGS contains very dense shell-supported matrices in some SubAggs (Wilkins et al., 2017), and a dense sample of stone artefacts including backed pieces; some of the smallest at PP5-6 made on quartz (Brown et al., 2012).

Intermittent, but dense, occupation continued from 70.2 to 68.6 ka during OBS2 whilst sea-levels continued to fall from 74 to 77 m BSL, increasing the distance to the coast from 19 to 23 km. Evidence for shellfish appears absent as it is decalcified (Karkanas et al., 2015) and backed pieces persist as a stone tool type (Wilkins et al., 2017). Vegetation changed from initially mixed C3-C4 back to C4 plants being common, coinciding with a change to stronger contributions from summer convective rains.

BAS South (68.4–67.9 ka) signals a change back to C3 dominated vegetation, but the influence of summer rainfall is still strong. This only changes in BAS North (67.9–65.3 ka) when winter rainfall again prevails as sea-levels keep falling towards the peak of MIS 4 at 65 ka (De Deckker et al., 2019). Phytoliths in BAS have the highest mean value of grasses amongst StratAggs (Esteban et al., 2020b), consistent with its location furthest away from the coast. The transition from the peak of MIS 4 when sea-level was at its lowest and the coast furthest away, to just before the start of sea-level transgression towards MIS 3, is characterised by a sandy layer with episodic occupation at the top of BAS (SubAgg Achilles; 65.3–64.9 ka) associated with a short switch-back to stronger summer rainfall.

The period 64.9–61.9 ka signals a period of sediment re-deposition and/or erosion. There is a break in sedimentation between BAS and BBCSR, and DBCS (66.7–60.6 ka; light blue bar in Fig. 14C) was moved through gravity flow processes to its current location (Fig. S15) where it truncated OBS2, SGS and OBS1 (Karkanas et al., 2015). Analyses of the single-grain D_e distributions for the three DBCS samples suggest that they maintained their integrity and that they likely date the timing of original deposition, rather than subsequent re-deposition. The bottom two SubAggs (Quinn and Sorel) gave ages consistent with BAS and SubAgg Miller at the top of DBCS gave an age consistent with BBCSR. DBCS is, therefore, a derivative of BAS and BBCSR. It is, therefore not 'filling the gap' between BAS and BBCSR, but rather brings the two together, consistent with an erosion event (cluster-b) at 61 ± 2 ka. This period of re-deposition and erosion was characterised by fluctuating vegetation and rainfall patterns during rising sea-levels at the end of MIS 4. The stone artefacts found in DBCS are consistent with the strict definition of the Howiesons Poort (HP) industry (Brown et al., 2012).

Occupation in BBCSR (61.9–59.7 ka) occurred during the final part of the sea-level transgression towards the end of MIS 4. This occupation is associated with more of a mixed vegetation, consistent with phytolith analyses that show a high presence of C4 panicoid grasses and low representation of phytoliths from the wood of trees and shrubs (Esteban et al., 2020b) and stronger winter rainfall. Distance to coast is now back to within the 10 km foraging radius for the first time since SADBS Upper and the shoreline changed back to longer sandy beaches, losing the wetlands and coastal lakes that characterised the previous ~10 ka of the much-expanded Palaeo-Agulhas Plain. Silcrete remains a dominant raw material type with relatively high frequencies of chert and low frequencies of quartzite and quartz. Backed and notched pieces are still present (Wilkins et al., 2017).

The start of MIS 3 coincides with RBSR South (59.7–56.4 ka). Sea-levels were relatively stable, first falling and then rising (53–60 to 55 m BSL) and the coast ~7–9 km distant. Vegetation is dominated by C3 plants and the influence of winter rainfall stronger. Occupation is only episodic and many of these deposits look like debris flows. BCS (57.7–53.7 ka; light green bar in Fig. 14C) overlaps with the top of RBSR South and the bottom of RBSR North (SubAgg Ellis) and post-dates BBCSR. BCS is like DBCS but located further to the north (Fig. S15) where it truncates OBS2 and consists of very black sediment layers, rich in archaeological remains. This contrasts with the episodic nature of RBSR South, but is consistent with SubAgg Ellis in RBSR North, also a debris flow. SubAgg Ellis unconformably overlies BBCSR in parts of the excavation and occurred during a period of sea-level rise (57–53 m BSL). BCS and SubAgg Ellis in RBSR North, therefore, signals the final occupation in PP5-6, but was not found in its primary depositional context. Like DBCS, the ages date the time of occupation, rather than re-deposition, and its start coincides with the cluster-c erosional event (57 ± 1 ka, Fig. 13C and D; grey bar in Fig. 14C). Occupation is capped by a sterile dune deposit in RBSR North. A later period of erosion (cluster-d; 41 ± 1 ka in Fig. 13C and D) resulted in the re-working and re-deposition of some materials.

6. Concluding remarks

In this study, we have demonstrated the systematic optical dating approach taken to construct a finely-resolved chronological framework for sediment deposition and occupation at PP5-6. The approach is time, labour and resource intensive and not feasible, or indeed practical, for application to all sites. It requires consistency between the scales of analysis, where the chronological resolution matches the stratigraphic resolution exposed through detailed excavation and recording of stratigraphy and plotted finds. The systematic dating approach starts in the field with sampling strategy, consideration of the quality and purpose of each sample, and any stratigraphic and taphonomic issues that may impact the reliability of the ages. It continues in the laboratory through each step of the measurement of D_e and dose rate, underpinned by a number of longitudinal studies to monitor the performance of different pieces of equipment. Ultimately it requires consideration of prior information, including independent age control, in the structure and error propagation for age modelling. It involves many iterations of sample measurement, analysis, testing and modelling. We demonstrated that where such requirements can be met, it is possible to increase the resolution and precision of optical dating chronologies down towards human timescales getting us closer to the resolution required to interrogate records in finer detail through time and compare it with other high-resolution global, regional and local records.

Sediment deposition at PP5-6 is closely tied to the rising (roofspall-dominated) and falling (aeolian-dominated) of sea-level. Changing sea-levels result in the expansion and contraction of the Palaeo-Agulhas Plain giving rise to changing environments and availability of new resources. This may then bring about changes in behaviour, demography and variations in resource use. At PP5-6, the start of microlithic technologies, change in preferred raw material from quartzite to silcrete, and the prolific use of heat treatment of silcrete to produce microliths occurs in SADBS dated to between 74.2 ± (1.5, 4.1) and 72.7 ± (1.4, 4.0) ka. This coincides with the first period of dense occupation characterised by palimpsests of combustion features signalling an occupation change from previously low intensity episodic and discrete occupation to high intensity, high frequency short visits. These changes in behaviour, technology, raw material use and demography immediately preceded and coincided with a period of unparalleled changes in sea-level (40 cm fall in sea-level per generation) and concomitant changes in climate and environment, showing the variety of interconnected causes and effects.

The chronological framework for Blombos Cave (BBC) followed the same systematic approach, so the PP5-6 and BBC chronologies can be directly compared. The M1 phase at BBC is associated with a fully

established, silcrete dominated Still Bay assemblage (Villa et al., 2009; Mourre et al., 2010; Archer et al., 2016), marine shell beads (Henshilwood et al., 2004) and engraved ochres (Henshilwood et al., 2002). The Still Bay at BBC overlaps with the silcrete dominated microlithic (backed artefacts) assemblage at PP5-6 found in SADBS Lower, SADBS Upper, OBS1 and SGS, but not with the 'classic' Howiesons Poort found in DBCS (and by inference BAS and BBCSR) (Brown et al., 2012) and at nearby Klipdrift shelter (Henshilwood et al., 2014). Like at PP5-6, occupation during the M1 phase at BBC is characterised by high intensity, high frequency short visits (Haaland et al., 2020). Such chronological overlaps now open up opportunities to directly compare and interrogate contemporaneous diachronic changes in technology and refine our understanding of the longer-term development of microlithic technologies, the meaning of the term Howiesons Poort, and the relationship between the Still Bay and Howiesons Poort (Jacobs et al., 2008a; Jacobs and Roberts, 2017).

A similar approach can be applied in other regions of the world where sites have sufficient and matching stratigraphic and chronological control.

CRediT authorship contribution statement

Zenobia Jacobs: Conceptualization, Methodology, Validation, Formal analysis, Investigation, Resources, Data curation, Writing – original draft, Visualization, Project administration, Funding acquisition. **Panagiotis Karkanas:** Conceptualization, Resources, Writing – review & editing. **B. Patrick Fahey:** Formal analysis, Resources, Data curation, Writing – review & editing, Visualization. **Erich C. Fisher:** Conceptualization, Formal analysis, Data curation, Writing – review & editing. **Curtis W. Marean:** Conceptualization, Resources, Data curation, Writing – review & editing, Supervision, Project administration, Funding acquisition.

Declaration of competing interest

The authors declare that they have no known competing financial interests or personal relationships that could have appeared to influence the work reported in this paper.

Acknowledgements

We would like to dedicate this paper to Professor Ann Wintle who had the vision to introduce single-grain OSL dating into the South African Middle Stone Age more than two decades ago. She never wavered in her support and encouragement of us and the project. Ann epitomises what it is to be a great scientist, but most importantly is just a great human being. Thank you for the journey of a lifetime.

This research was funded by grants and fellowships awarded to Z.J. from the Australian Research Council. We thank all members of the University of Wollongong Optical Dating Facility. Specifically, we would like to acknowledge Richard G. Roberts and Bo Li who have spearheaded many of the optical dating method developments used in this study and Bo Li for his development of R scripts for reproducible analyses of these large datasets. Terry Lachlan is thanked for his unwavering commitment to quality assurance of the equipment and operations of the laboratory, including biosecurity, for as long as this project has been in progress. Yasaman Jafari and Lili Yu for overseeing the day-to-day operations of the laboratory and for preparing all these samples, and all other members of the laboratory (past and present) that assisted with preparation of the samples.

CWM recognizes the support of grants from the National Science Foundation (BCS-0524087, BCS-1138073 and BCS-1460376), Hyde Family Foundations, the Institute of Human Origins (IHO) at Arizona State University, and the John Templeton Foundation to the Institute of Human Origins at Arizona State University. The opinions expressed in this publication are those of the author(s) and do not necessarily reflect the views of any of these funding organizations.

Appendix A. Supplementary data

Supplementary data to this article can be found online at https://doi.org/10.1016/j.quascirev.2025.109263.

Data availability

All data and/or code is contained within the submission.

References

Aitken, M.J., 1998. An Introduction to Optical Dating. Oxford University Press, Oxford.
Allsopp, N., Colville, J.F., Verboom, G.A., 2014. Fynbos: Ecology, Evolution, and Conservation of a Megadiverse Region. Oxford University Press, Oxford.
Archer, W., Pop, C.M., Gunz, P., McPherron, S.P., 2016. What is the Still Bay? Human biogeography and bifacial point variability. J. Hum. Evol. 97, 58–72.
Athanassas, C., Wagner, G., 2016. Geochronology beyond Radiocarbon: optically stimulated luminescence dating of palaeoenvironments and archaeological sites. Elements 12, 27–32.
Bar-Matthews, M., Marean, C.W., Jacobs, Z., Karkanas, P., Fisher, E.C., Herries, A.I.R., Brown, K.S., Williams, H.M., Bernatchez, J., Ayalon, A., Nilssen, P.J., 2010. A high resolution and continuous isotopic speleothem record of paleoclimate and paleoenvironment from 90 to 53 ka from Pinnacle Point on the south coast of South Africa. Quat. Sci. Rev. 29, 2131–2145.
Bateman, M.D., Holmes, P.J., Carr, A.S., Horton, B.P., Jaiswal, M.K., 2004. Aeolianite and barrier dune construction spanning the last two glacial-interglacial cycles from the southern Cape Coast, South Africa. Quat. Sci. Rev. 23, 1681–1698.
Bernatchez, J., Marean, C.W., 2011. Total station archaeology and the use of digital photography. SAA Archaeol. Rec. 11, 16–21.
Braun, K., Bar Matthews, M., Matthews, A., Ayalon, A., Zilberman, T., Cowling, R.M., Fisher, E.C., Herries, A.I.R., Brink, J.S., Marean, C.W., 2020. Comparison of climate and environment on the edge of the Palaeo-Agulhas Plain to the Little karoo (South Africa) in marine isotope stages 5–3 as indicated by speleothems. Quat. Sci. Rev. 235, 105803.
Braun, K., Bar-Matthews, M., Matthews, A., Ayalon, A., Cowling, R.M., Karkanas, P., Fisher, E.C., Dyez, K., Zilberman, T., Marean, C.W., 2019. Late Pleistocene records of speleothem stable isotopic compositions from Pinnacle Point on the South African south coast. Quat. Res. 91, 265–288.
Bronk Ramsey, C., 2009a. Bayesian analysis of radiocarbon dates. Radiocarbon 51, 337–360.
Bronk Ramsey, C., Dee, M., Lee, S., Nakagawa, T., Staff, R., 2010. Developments in the calibration and modelling of radiocarbon dates. Radiocarbon 52, 953–961.
Bronk Ramsey, C., Lee, S., 2013. Recent and planned developments of the program OxCal. Radiocarbon 55, 720–730.
Brown, K.S., Marean, C.W., Herries, A.I.R., Jacobs, Z., Tribolo, C., Braun, D., Roberts, D. L., Meyer, M.C., Bernatchez, J., 2009. Fire as an engineering tool of early modern humans. Science 325, 859–862.
Brown, K.S., Marean, C.W., Jacobs, Z., Schoville, B.J., Oestmo, S., Fisher, E.C., Bernatchez, J., Karkanas, P., Matthews, T., 2012. An early and enduring advanced technology originating 71,000 years ago in South Africa. Nature 491, 590–594.
Carr, A.S., Bateman, M.D., Roberts, D.L., Murray-Wallace, C.V., Jacobs, Z., Holmes, P.J., 2010. The last interglacial sea-level high stand on the southern Cape coastline of South Africa. Quat. Res. 73, 351–363.
Carr, A.S., Chase, B.M., Mackay, A., 2016. Mid to late Quaternary landscape and environmental dynamics in the Middle Stone Age of southern South Africa. Vertebrate Paleobiology and Palaeoanthropology 23–47.
Cawthra, H.C., Jacobs, Z., Compton, J.S., Fisher, E.C., Karkanas, P., Marean, C.W., 2018. Depositional and sea-level history from MIS 6 (Termination II) to MIS 3 on the southern continental shelf of South Africa. Quat. Sci. Rev. 181, 156–172.
Cawthra, H.C., Anderson, R.J., De Vynck, J.C., Jacobs, Z., Jerardino, A., Kyriacou, K., Marean, C.W., 2020. Migration of Pleistocene shorelines across the Palaeo-Agulhas Plain: evidence from dated sub-bottom profiles and archaeological shellfish assemblages. Quat. Sci. Rev. 235, 106107.
Chen, G., Murray, A.S., Li, S.-H., 2001. Effect of heating on the quartz dose-response curve. Radiat. Meas. 33, 59–63.
Clark, J.D., 1985. In: Misra, V.N., Bellwood, P. (Eds.), Recent Advances in Indo-Pacific Prehistory. E. J. Brill, pp. 95–101.
Cowling, R.M., Potts, A.J., Bradshaw, P.L., Colville, J., Arianoutsou, M., Ferrier, S., Forest, F., Fyllas, N.M., Hopper, S.D., Ojeda, F., Proches, S., Smith, R.J., 2015. Variation in plant diversity in Mediterranean-climate ecosystems: the role of climatic and topographical stability. J. Biogeogr. 42, 552–564.
De Deckker, P., Arnold, L.J., Van der Kaars, S., Bayon, G., Stuut, J.W., Perner, K., Lopes dos Santos, R., Uemura, R., Demuro, M., 2019. Marine Isotope Stage 4 in Australasia: a full glacial culminating 65,000 years ago —global connections and implications for human dispersal. Quat. Sci. Rev. 2019, 187–207.
Duller, G.A.T., Bøtter-Jensen, L., Murray, A.S., 2000. Optical dating of single sand-sized grains of quartz: sources of variability. Radiat. Meas. 32, 453–457.
Esteban, I., Albert, R.M., Cabanes, D., Marean, C.W., 2020a. Estratègies de recol· lecció de plantes i paleoambients durant la Middle Stone Age a Pinnacle Point (costa sud de Sud-àfrica): les anàlisis de fitòlits. Tribuna d'Arqueologia 29–51.

Esteban, I., Marean, C.W., Cowling, R.M., Fisher, E.C., Cabanes, D., Albert, R.M., 2020b. Palaeoenvironments and plant availability during MIS 6 to MIS 3 on the edge of the Palaeo-Agulhas Plain (south coast, South Africa) as indicated by phytolith analysis at Pinnacle Point. Quat. Sci. Rev. 235, 105667.
Fenner, J.N., 2005. Cross-cultural estimation of the human generation interval for use in genetics-based population divergence studies. Am. J. Phys. Anthropol. 128, 415–423.
Fisher, E.C., Bar-Matthews, M., Jerardino, A., Marean, C.W., 2010. Middle and Late Pleistocene paleoscape modeling along the southern coast of South Africa. Quat. Sci. Rev. 29, 1382–1398.
Fisher, E.C., Akkaynak, D., Jacob, H., Herries, A.I.R., Jacobs, Z., Karkanas, P., Marean, C. W., McGrath, J.R., 2015. Technical considerations and methodology for creating high-resolution, color-corrected, and georectified photomosaics of stratigraphic sections at archaeological sites. J. Archaeol. Sci. 57, 380–394.
Fisher, E.C., Cawthra, H.C., Esteban, I., Jerardino, A., Neumann, F.H., Oertle, A., Pargeter, J., Saktura, R.B., Szabo, K., Winkler, S., Zohar, I., 2020. Coastal occupation and foraging during the last glacial maximum and early Holocene at Waterfall Bluff, eastern Pondoland, South Africa. Quat. Res. 97, 1–41.
Galbraith, R.F., 2003. A simple homogeneity test for estimates of dose obtained using OSL. Ancient TL 21, 75–78.
Galbraith, R.F., Roberts, R.G., Laslett, G.M., Yoshida, H., Olley, J.M., 1999. Optical dating of single and multiple grains of quartz from Jinmium rock shelter, Northern Australia: part 1, experimental design and statistical models. Archaeometry 41, 339–364.
Galbraith, R.F., Roberts, R.G., 2012. Statistical aspects of equivalent dose and error calculation and display in OSL dating: an overview and some recommendations. Quat. Geochronol. 11, 1–27.
Göktürk, O.M., Simon, M.H., Sobolowski, S.P., Zhang, Z., Van der Bilt, W., Morkved, P.T., D'Andrea, W.J., Van Niekerk, K.L., Henshilwood, C.S., Armitage, S.J., Jansen, E., 2023. Behaviourally modern humans in coastal southern Africa experienced an increasingly continental climate during the transition from Marine Isotope Stage 5 to 4. Front. Earth Sci. 11, 1198068.
Haaland, M.M., Miller, C.E., Unhammer, O.F., Reynard, J.P., Van Niekerk, K.L., Ligouis, B., Mentzer, S.M., Henshilwood, C.S., 2020. Geoarchaeological investigations of occupation deposits in Blombos Cave in South Africa indicate changes in site use and settlement dynamics in the southern Cape during MIS 5b–4. Quat. Res. 100, 170–223.
Helm, C.W., Cawthra, H.C., Cowling, R.M., De Vynck, J.C., Lockley, M.G., Marean, C.W., Thesen, G.H.H., Venter, J.A., 2020. Pleistocene vertebrate tracksites on the Cape south coast of South Africa and their potential palaeoecological implications. Quat. Sci. Rev. 235, 105857.
Henshilwood, C.S., D'Errico, F., Yates, R., Jacobs, Z., Tribolo, C., Duller, G.A.T., Mercier, N., Sealy, J.C., Valladas, H., Watts, I., Wintle, A.G., 2002. Emergence of modern human behavior: middle Stone Age engravings from South Africa. Science 295, 1278–1280.
Henshilwood, C.S., d'Errico, F., Vanhaeren, M., Van Niekerk, K., Jacobs, Z., 2004. Middle stone age shell beads from South Africa. Science 304, 404.
Henshilwood, C.S., Van Niekerk, K.L., Wurz, S., Delagnes, A., Armitage, S.J., Difkin, R.F., Douze, K., Keene, P., Haland, M.M., Reynard, J., Discamps, E., Mienies, S.S., 2014. Klipdrift shelter, southern Cape, South Africa: preliminary report on the Howiesons Poort layers. J. Archaeol. Sci. 45, 284–303.
Huntley, D.J., Godfrey-Smith, D.I., Thewalt, M.L.W., 1985. Optical dating of sediments. Nature 313, 105–107.
Jacobs, Z., 2010. An OSL chronology for the sedimentary deposits from Pinnacle Point Cave 13B—a punctuated presence. J. Hum. Evol. 59, 289–305.
Jacobs, Z., Roberts, R.G., 2007. Advances in optically stimulated luminescence dating of individual grains of quartz from archeological deposits. Evol. Anthropol. 16, 210–223.
Jacobs, Z., Roberts, R.G., 2017. Single-grain OSL chronologies for the Still Bay and Howieson's Poort industries and the transition between them: further analyses and statistical modelling. J. Hum. Evol. 107, 1–13.
Jacobs, Z., Duller, G.A.T., Wintle, A.G., 2006. Interpretation of single grain D_e distributions and calculation of D_e. Radiat. Meas. 41, 264–277.
Jacobs, Z., Roberts, R.G., Galbraith, R.F., Deacon, H.J., Grün, R., Mackay, A., Mitchell, P., Vogelsang, R., Wadley, L., 2008a. Ages for the Middle Stone Age of southern Africa: implications for human behavior and dispersal. Science 322, 733–735.
Jacobs, Z., Wintle, A.G., Duller, G.A.T., Roberts, R.G., Wadley, L., 2008b. New ages for the post-Howiesons Poort, late and final Middle Stone Age at Sibudu, South Africa. J. Archaeol. Sci. 35, 1790–1807.
Jacobs, Z., Li, B., Shunkov, M.V., Kozlikin, M.B., Bolikhovskaya, N.S., Agadjanian, A.K., Uliyanov, V.A., Vasiliev, S.K., O'Gorman, K., Derevianko, A.P., Roberts, R.G., 2019. Timing of archaic hominin occupation of Denisova Cave in southern Siberia. Nature 565, 594–599.
Jacobs, Z., Jones, B.G., Cawthra, H.C., Henshilwood, C.S., Roberts, R.G., 2020. The chronological, sedimentary and environmental context for the archaeological deposits at Blombos Cave, South Africa. Quat. Sci. Rev. 235, 105850.
Karkanas, P., Brown, K.S., Fisher, E.C., Jacobs, Z., Marean, C.W., 2015. Interpreting human behaviour from depositional rates and combustion features through the study of sedimentary microfacies at site Pinnacle Point 5-6, South Africa. J. Hum. Evol. 85, 1–21.
Karkanas, P., Marean, C., Bar-Matthews, M., Jacobs, Z., Fisher, E., Braun, K., 2020. Cave life histories of non-anthropogenic sediments help us understand associated archaeological contexts. Quat. Res. 99, 270–289.
Kuhn, S., 2002. Pioneers of microlithization: the "proto-Aurignacian" of Southern Europe. Archaeological Papers of the American Anthropological Association 12, 83–94.
Li, B., Jacobs, Z., Roberts, R.G., Galbraith, R., Peng, J., 2017. Variability in quartz OSL signals caused by measurement uncertainties: problems and solutions. Quat. Geochronol. 41, 11–25.
Li, B., Jacobs, Z., Roberts, R.G., 2020. Validation of the L_nT_n method for D_e determination in optical dating of K-feldspar and quartz. Quat. Geochronol. 58, 101066.
Lisiecki, L.E., Raymo, M.E., 2005. A Pliocene-Pleistocene stack of 57 globally distributed benthic $\delta^{18}O$ records. Palaeooceanography 20, PA1003.
Manning, J.C., Goldblatt, P., 2012. Plants of the Greater Cape Floristic Region, Streletzia. South African National Biodiversity Institute, Pretoria.
Marean, C.W., Bar-Matthews, M., Bernatchez, J., Fisher, E., Goldberg, P., Herries, A.I.R., Jacobs, Z., Jerardino, A., Karkanas, P., Minichillo, T., Nilssen, P.J., Thompson, E., Watts, I., Williams, H.W., 2007. Early human use of marine resources and pigment in South Africa during the Middle Pleistocene. Nature 449, 905–908.
Marean, C.W., 2010. Pinnacle Point Cave 13B (Western Cape Province, South Africa) in context: the Cape floral kingdom, shellfish, and modern human origins. J. Hum. Evol. 59, 425–433.
Marean, C.W., Cawthra, H.C., Cowling, R.C., Esler, K.J., Fisher, E., Milewski, A., Potts, A. J., Singels, E., De Vynck, J., 2014. Stone age people in a changing South African greater Cape floristic region. In: Allsopp, N., Colville, J.F., Verboom, T. (Eds.), Ecology and Evolution of Fynbos: Understanding Megadiversity. Oxford University Press, Oxford, pp. 164–199.
Marean, C.W., 2015. An evolutionary anthropological perspective on modern human origins. Annu. Rev. Anthropol. 44, 533–556.
Marean, C.W., Cowling, R.M., Franklin, J., 2020. The Palaeo-Agulhas Plain: temporal and spatial variation in an extraordinary extinct ecosystem of the Pleistocene of the Cape floristic region. Quat. Sci. Rev. 235, 106161.
Marlowe, F.W., 2005. Hunter-gatherers and human evolution. Evol. Anthropol. 14, 54–67.
Matthews, T., Marean, C.W., Cleghorn, N., 2020. Past and present distributions and community evolution of Muridae and Soricidae from MIS 9 to MIS 1 on the edge of the Palaeo-Agulhas Plain (south coast, South Africa). Quat. Sci. Rev. 235, 105774.
McGrath, J.R., MacDonald, B.L., Stalla, D., 2022. Middle stone age mineral pigment procurement at Pinnacle point 5–6 north, western Cape province, South Africa. Archaeometry 64, 193–217.
Mourre, V., Villa, P., Henshilwood, C.S., 2010. Early use of pressure flaking on lithic artifacts at Blombos Cave, South Africa. Science 330, 659–662.
Murray, A.S., Arnold, L.J., Buylaert, J., Guerin, G., Qin, J., Singhvi, A.K., Smedley, R., Thomsen, K.J., 2021. Optically stimulated luminescence dating using quartz. Nature Reviews Methods Primers 1, 72.
Oestmo, S., Schoville, B.J., Wilkins, J., Marean, C.W., 2014. A middle stone age paleoscape near the Pinnacle point caves, vleesbaai, South Africa. Quat. Int. 350, 147–168.
Oldham, P.D., 1962. A note on the analysis of repeated measurements of the same subjects. J. Chron. Dis. 15, 969–977.
Powell, R., Hergt, J., Woodhead, J., 2002. Improving isochron calculations with robust statistics and the bootstrap. Chem. Geol. 185, 191–204.
Rhodes, E.J., Bronk Ramsey, C., Outram, Z., Batt, C., Willis, L., Dockrill, S., Bond, J., 2003. Bayesian methods applied to the interpretation of multiple OSL dates: high precision sediment ages from Old Scatness Broch excavations, Shetland Isles. Quat. Sci. Rev. 22, 1231–1244.
Roberts, D.L., Karkanas, P., Jacobs, Z., Marean, C.W., Roberts, R.G., 2012. Melting ice sheets 400,000 yr ago raised sea level by 13 m: past analogue for future trends. Earth Planet Sci. Lett. 357–358, 226–237.
Roberts, R.G., Galbraith, R.F., Olley, J.M., Yoshida, H., Laslett, G.M., 1999. Optical dating of single and multiple grains of quartz from Jinmium Rock Shelter, northern Australia: part II, results and implications. Archaeometry 41, 365–395.
Roberts, R.G., Jacobs, Z., Li, B., Jankowski, N.R., Cunningham, A.C., Rosenfeld, A.B., 2015. Optical dating in archaeology: thirty years in retrospect and grand challenges for the future. J. Archaeol. Sci. 56, 41–60.
Roberts, R.G., Galbraith, R.F., Yoshida, H., Laslett, G.M., Olley, J.M., 2000. Distinguishing dose populations in sediment mixtures: a test of single-grain optical dating procedures using mixtures of laboratory-dosed quartz. Radiat. Meas. 32, 459–465.
Rousseeuw, P.J., Debruyne, M., Engelen, S., Hubert, M., 2006. Robustness and outlier detection in chemometrics. Crit. Rev. Anal. Chem. 36, 221–242.
Smith, E., Jacobs, Z., Johnsen, R., Ren, M., Fisher, E.C., Oestmo, S., Wilkins, J., Harris, J. A., Karkanas, P., Fitch, S., Ciravolog, A., Keenan, D., Cleghorn, N., Lane, C.S., Matthews, T., Marean, C.W., 2018. Humans thrived in South Africa through the Toba super-volcanic eruption ~74 000 years ago. Nature 555, 511–515.
Storey, M., Roberts, R.G., Saidin, M., 2012. Astronomically calibrated $^{40}Ar/^{39}Ar$ age for the Toba super-eruption and global synchronization of late Quaternary records. Proceedings of the National Academy of Sciences of the USA 109, 18684–18688.
Villa, P., Soressi, M., Henshilwood, C.S., Mourre, V., 2009. The still Bay points of Blombos cave (South Africa). J. Archaeol. Sci. 36, 441–460.
Wadley, L., 2015. Those marvellous millennia: the middle stone age of southern Africa. Azania 50, 155–226.
Waelbroeck, C., Labeyrie, L., Michel, E., Duplessy, J.C., McManus, J.F., Lambeck, K., Balbon, E., Labracherie, M., 2002. Sea-level and deep water temperature changes derived from benthic foraminifera isotopic records. Quat. Sci. Rev. 21, 295–305.

Wilkins, J., Brown, K.S., Oestmo, S., Pereira, T., Ranhorn, K.L., Schoville, B.J., Marean, C. W., 2017. Lithic technological responses to late Pleistocene glacial cycling at Pinnacle point site 5-6, South Africa. PLoS One 12, e0174051.
Wintle, A.G., 2014. Luminescence dating methods. In: Holland, H.D., Turekian, K.K. (Eds.), Treatise on Geochemistry, second ed. 14. Elsevier, Oxford, pp. 17–35.
Wood, R., Jacobs, Z., Vannieuwenhuyse, D., Balme, J., O'Connor, S., Whitau, R., 2016. Towards an accurate and precise chronology for the colonization of Australia: the example of Riwi, Kimberley, Western Australia. PLoS One 11, e0160123.